

Microfluidic Platforms for the Separation of Particles

by

Ricardo Ortiz

A Thesis Presented in Partial Fulfillment
of the Requirements for the Degree
Master of Science

Approved October 2021 by the
Graduate Supervisory Committee:

Alexandra Ros, Chair
Mark Hayes
Chad Borges

ARIZONA STATE UNIVERSITY

December 2021

ABSTRACT

Microfluidic platforms have been exploited extensively as a tool for the separation of particles by electric field manipulation. Microfluidic devices can facilitate the manipulation of particles by dielectrophoresis. Separation of particles by size and type has been demonstrated by insulator-based dielectrophoresis in a microfluidic device. Thus, manipulating particles by size has been widely studied throughout the years. It has been shown that size-heterogeneity in organelles has been linked to multiple diseases from abnormal organelle size.

Here, a mixture of two sizes of polystyrene beads (0.28 and 0.87 μm) was separated by a ratchet migration mechanism under a continuous flow (20 nL/min). Furthermore, to achieve high-throughput separation, different ratchet devices were designed to achieve high-volume separation. Recently, enormous efforts have been made to manipulate small size DNA and proteins. Here, a microfluidic device comprising of multiple valves acting as insulating constrictions when a potential is applied is presented. The tunability of the electric field gradient is evaluated by a COMSOL model, indicating that high electric field gradients can be reached by deflecting the valve at a certain distance. Experimentally, the tunability of the dynamic constriction was demonstrated by conducting a pressure study to estimate the gap distance between the valve and the substrate at different applied pressures. Finally, as a proof of principle, 0.87 μm polystyrene beads were manipulated by dielectrophoresis. These microfluidic platforms will aid in the understanding of size-heterogeneity of organelles for biomolecular assessment and achieve separation of nanometer-size DNA and proteins by dielectrophoresis.

DEDICATION

I would like to dedicate this work to my parents. I will never be able to repay all the sacrifices you made for my brothers and me. I would also like to dedicate my work to my *abuelita*, but COVID-19 won the battle. You are now with MF Doom and O.D.B. To my extended family in the US and Mexico for all the memories. To Juliana, thank you for your patience, the laughs, and the company. Next, I would like to dedicate this work to my childhood friends, “we made it out of the hood.” Also, dedicated to all the minorities out there struggling to have an education and first-generation immigrants, this work is also dedicated to you. Finally, I would like to end this dedication with one of my favorite phrases by the magnificent Paco Aguilar, “*La vida es un riesgo, carnal!*”

ACKNOWLEDGMENTS

First, I would like to gratefully thank Dr. Alexandra Ros for mentoring me throughout my research experience. I would like to thank the Ros lab for all the help in my research in microfabrication, experiments, COMSOL, and dielectrophoresis theory. I would also like to thank them for all the beers and potlucks. Finally, I would like to thank other graduate students for their friendship as well.

TABLE OF CONTENTS

| | Page |
|--|------|
| LIST OF TABLES..... | vi |
| LIST OF FIGURES | vii |
| CHAPTER | |
| 1 INTRODUCTION | 1 |
| 2 BACKGROUND AND THEORY | 4 |
| 2.1. Transport Phenomena in the Microenvironment..... | 4 |
| 2.2. Electrokinetic Transport Phenomena..... | 6 |
| 3 A CONTINUOUS HIGH THROUGHPUT INSULATOR-BASED DIELECTROPHORESIS DEVICE FOR SIZE-BASED PARTICLE SEPARATION | 11 |
| 3.1. Introduction..... | 10 |
| 3.2. Experimental Details | 13 |
| 3.3. Results and Discussion..... | 16 |
| 3.4. Conclusion and Future Direction | 24 |
| 4 A TUNABLE INSULATOR-BASED DIELECTROPHORESIS SYSTEM FOR THE SEPARATION OF PARTICLES..... | 25 |
| 4.1. Introduction..... | 25 |
| 4.2. Experimental Section | 27 |
| 4.3. Results and Discussion..... | 30 |
| 4.4. Conclusion and Future Work | 39 |
| 5 CONCLUSION AND FUTURE DIRECTIONS..... | 41 |

| CHAPTER | Page |
|--|------|
| REFERENCES | 43 |
| APPENDIX | |
| A COMSOL SIMULATION DETAILS FOR CHAPTER 4 | 55 |

LIST OF TABLES

| Table | Page |
|--|------|
| 1. Dimension of the Control and Fluidic Channels | 28 |

LIST OF FIGURES

| Figure | Page |
|---|------|
| 1. Schematic Illustration of Laminar Flow in a Circular Capillary | 5 |
| 2. Schematic Illustration of Electric Double Layer and Electroosmotic Flow | 8 |
| 3. Schematic of an Electrophoretic Force Acting on a Particle | 9 |
| 4. Schematic Image of the Ratchet Device, Sem Image of the Ratchet Post Dimension, Waveforms Applied for Ratchet Migration, and Electric Field Distribution Obtained from Numerical Model | 17 |
| 5. Illustration of the Theoretical Migration in the Device..... | 20 |
| 6. Velocity Variation of 0.28 and 0.87 μm Diameter Polystyrene Beads Across the Microfluidic Channel | 22 |
| 7. Schematic Overview of the Contact, Contactless, and Continuous Devices and Optical Images of Injected Gallium | 23 |
| 8. Schematic Representation of Microfluidic Device | 28 |
| 9. Schematic of Comsol Geometry and Electric Field Values Calculated from the Comsol Model..... | 31 |
| 10. Schematic Representation and Fluorescence Microscope Pictures of a Normally Closed Valve in Open and Closed Position | 32 |
| 11. Pressure Threshold Versus Aspect Ratio and Valve Location | 33 |
| 12. Calibration Curve Acquired from the Measurement of Different Channel Heights Filled with a Fluorescence Dye and Calculated Distances from the Calibration Curve | 35 |

| Figure | Page |
|---|------|
| 13. Schematics Representing Polystyrene Beads Subjected to Different Electrical Parameters and Valves Subjected to Different Pneumatic Pressures..... | 37 |
| 14. Intensity Variations by Different Applied Pressures..... | 36 |

CHAPTER 1

INTRODUCTION

Separation science has been a major tool in analytical chemistry. Separation techniques such as electrophoresis (EP) have been used to separate DNA and proteins. Organelles such as mitochondria have mainly been separated by differential centrifugation or density gradient centrifugation. Lately, dielectrophoresis has been proposed to be an excellent tool for the separation of analytes. This electrokinetic technique has been combined with the robustness of microfluidic devices made out of polydimethylsiloxane (PDMS) to achieve particle manipulation. Insulator-based dielectrophoresis (iDEP) uses insulating structures to generate nonuniform electric fields across the channel. In this thesis, different types of microfluidic platforms were developed to manipulate particles and, in the future, to be applied to biomolecules and organelles.

Manipulation of DNA has gained significant attention for vast technological applications such as information storage¹ and computing² as well as health applications such as vaccines³ and prognostics.⁴ Electrophoresis is the primary separation technique for the separation of DNA. Agarose gel and capillary EP are the preferred methods to separate DNA fragments.^{5,6} However, the manipulation of DNA by DEP has also been demonstrated.^{7,8} In the case of DNA subjected to a DEP force, the polarization mechanism of the DNA molecule in an electrolyte solution subjected to a nonuniform electric field is not well understood. However, the commonly accepted polarization mechanism is the so-called counter ion polarization.⁹ Nevertheless, DEP theoretical models for DNA have matched with experimental responses of kbp and rod-like DNA

structures.^{10, 11} In addition, different groups have demonstrated the manipulation of DNA by iDEP. These approaches were achieved by microfabricating different microfluidic channel geometries such as nanoslits¹² and circular insulating posts.¹³ Although many efforts have been made to manipulate small-size analytes, the challenge still remains to manipulate small-size biomolecules by DEP. This challenge arises due to the DEP scaling factor, where the force scales with the polarization and size of the analyte. Hence, manipulating bioanalytes by DEP might require large potentials for the biomolecules to be manipulated by DEP force. One standard method to increase the DEP force is by microfabricating insulating barriers to generate high electric fields.¹⁴ However, a drawback of these devices is the lack of tunability due to their fabrication method, where the insulating posts are static (i.e cannot be altered once fabricated).

Since microfluidics take advantage of simple fabrication processes (i.e, photolithography and soft lithography), one can introduce a dynamic valve that may act as an insulating constriction to fine-tune the electric field. One approach is to introduce pneumatic valves. A pneumatic valve is based on a flexible thin membrane that is pushed up or down by pressure or vacuum. Since a nonuniform electric field is required to induce a DEP force, the pneumatic valve can act as a flexible insulating constriction that generates a gap distance ($<1\mu\text{m}$) to achieve large electric fields with low electric potentials applied. Some groups have explored the concept of introducing pneumatic valves for sample manipulation. For example, Sabbagh et al.¹⁵ and Kwon et al.¹⁶ microfabricated a normally-open valve to preconcentrate analytes by electrokinesis. Here, a normally-closed valve is microfabricated in a microfluidic device to manipulate particles. The valve is designed to achieve sub-micrometer gap distances between the

valve and the glass substrate. Continually, developing a microfluidic device with multiple insulating valves can give a tunable microfluidic platform that can be exploited for multiple analytes by tailoring the potentials and valve actuation.

Resolving the subpopulations of mitochondria is important since abnormal sizes in mitochondria have been linked to different pathological issues such as Parkinson's disease.¹⁷ Mitochondria are typically separated by centrifugation techniques such as differential centrifugation¹⁸ and density gradient centrifugation.¹⁹ Recently, ratchet migration has been demonstrated to be a good candidate for the separation of mitochondria where a periodic potential is applied to an asymmetrical post geometry to induce separation.^{20, 21} This approach coupled with DEP has been demonstrated for the manipulation of mitochondria and liposomes.²² However, this work was lacking high throughput separation since no external flow was applied to the system. Therefore, developing a ratchet microfluidic device under a continuous flow is required for high throughput sample collection.

In this thesis, two microfluidic platforms for particle separation are discussed: a ratchet device and a tunable valve. Chapter 2 reviews the main physical phenomena in a microfluidic device and electrokinetic forces acting on a particle. Chapter 3 introduces a ratchet mechanism under a continuous flow for the separation of polystyrene beads. Chapter 4 introduces a novel microfluidic device that uses a normally-closed valve that acts as an insulating constriction when an electrical potential is applied. Finally, Chapter 5 concludes the thesis and suggests the future work for each project presented here.

CHAPTER 2

BACKGROUND AND THEORY

2.1. Transport Phenomena in the Microenvironment

2.1.1. Navier-Stokes Equation

The Navier-Stokes equation describes the flow of an incompressible Newtonian fluid with a constant viscosity, η . The Navier-Stokes equation can be expressed as:²³

$$\rho \left[\frac{\partial \mathbf{u}}{\partial t} + (\mathbf{u} \cdot \nabla) \mathbf{u} \right] = -\nabla p + \eta \cdot \nabla^2 \mathbf{u} + \mathbf{F} \quad (1)$$

where ρ is the fluid density, \mathbf{u} is the fluid velocity, ∇ is the gradient differential operator, p the pressure field, η is the viscosity of the medium, ∇^2 is the Laplacian operator, and \mathbf{F} is an external acceleration force (e.g., gravity or force due to an external electric field).

The left side of the equation corresponds to the inertial forces, and the right hand corresponds to the fluid pressure, fluid dynamic viscosity, and external forces applied to the fluid. The term $(\mathbf{u} \cdot \nabla) \mathbf{u} = 0$ is eliminated from the equation since an incompressible fluid is assumed and the equation reduces to:^{23, 24}

$$\rho \left[\frac{\partial \mathbf{u}}{\partial t} \right] = -\nabla p + \eta \cdot \nabla^2 \mathbf{u} + \mathbf{F} \quad (2)$$

2.1.2. Hagen-Poiseuille Equation

The Hagen-Poiseuille equation describes the pressure drop in a microchannel. Considering a laminar flow in a circular channel, the maximum velocity is at the center of the channel, and the velocity is zero at the wall (Figure 1). This is because the velocity between the wall and liquid is equal to the velocity of a solid ($v = 0$).²⁵

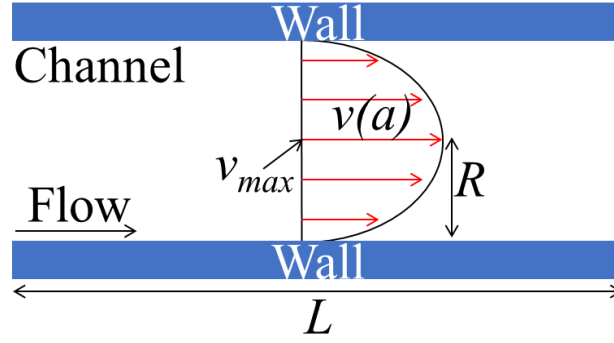


Figure 1. Schematic illustration of laminar flow in a circular channel. The flow is from left to right. The maximum velocity is at the center of the flow profile, and the velocity is zero at the wall.

The velocity $v(a)$ from zero at the wall to the maximum velocity at the centerline of the channel can be expressed as follows:²⁵

$$v(a) = \frac{\Delta p}{4\eta L} (R^2 - a^2), \text{ where } 0 < a < R \quad (3)$$

where Δp is the pressure difference across the fluidic channel, η viscosity of the medium, L is the length of the channel, and R is the radius of the channel. The maximum velocity at the centerline can be expressed by deriving equation 3 at $a = 0$. The equation is as follows:²⁵

$$v_{max} = \frac{\Delta p R^2}{4\eta L} \quad (4)$$

Finally, the pressure difference in a microchannel can also be expressed by considering the average velocity in the channel ($v_{ave} = \frac{1}{2} v_{max}$) and the volumetric flow rate ($Q = v_{ave} R^2 \pi$). Equating these two expressions into equation 4, we get an equation relating the pressure difference and the flow rate with the hydraulic resistance, R_{hydr} . The expression is as follows:²⁵

$$\Delta p = R_{hydr} Q = \frac{8\eta L}{\pi R^4} Q \quad (5)$$

2.2. Electrokinetic Transport Phenomena

2.2.1. Electroosmosis

The electroosmotic flow (EOF) is the phenomenon of a bulk flow of liquid in a channel when an electric field is applied.²⁶ In a PDMS microfluidic channel, the walls in the fluidic channel have negative charges due to the deprotonation of the silanol groups when exposed to plasma treatment.²⁷ At an applied potential a the so-called electric double layer (EDL) is created. Figure 2a shows a schematic of EDL. The y-axis represents the electric potential (ψ) and is defined as:²⁸

$$\psi(x) = \zeta e^{-x/\lambda_D} \quad (6)$$

where ζ is the zeta potential and λ_D is the Debye-Hückel length, The λ_D determines the thickness of the EDL. The thickness is expressed as:²⁴

$$\lambda_D = \sqrt{\frac{\epsilon_m k_B T}{2(Ze_c)^2 c_0}} \quad (7)$$

where ϵ_m is the permittivity of the medium, k_B is the Boltzmann constant, T is temperature, Z is the ion charge, e_c is the elementary charge, and c_0 is the electrolyte concentration. The negative charges on the walls are bound with the positive ions in the medium forming the Stern layer. The resulting ion bonding creates a layer with a higher positive ion concentration that is termed the Diffuse layer. The immobile layer between the wall and the medium is called the Stern layer. The free ions next to the Stern layer is termed the Diffuse layer. The Stern and Diffuse layer together are termed electrical double layer (EDL). Upon applying an electric field, the ions in the EDL move and

generate a flow leading to the liquid motion in the channel. The resulting is a flat profile at the cross section, and the velocity is zero at the wall (Figure 2b). The electroosmotic velocity, v_{eo} , is defined by:²⁹

$$v_{eo} = \mu_{eof} \mathbf{E} \quad (8)$$

where μ_{eof} is the electroosmotic mobility. The μ_{eof} is defined as:²⁹

$$\mu_{eof} = \frac{\varepsilon_m \zeta}{4\pi\eta} \quad (9)$$

where ε_m is the permittivity of the medium, ζ is the zeta potential, and η is the medium viscosity. The ζ is termed as:

$$\zeta = \frac{\lambda_D \sigma}{\varepsilon_m} \quad (10)$$

where σ is the charge density at the surface.

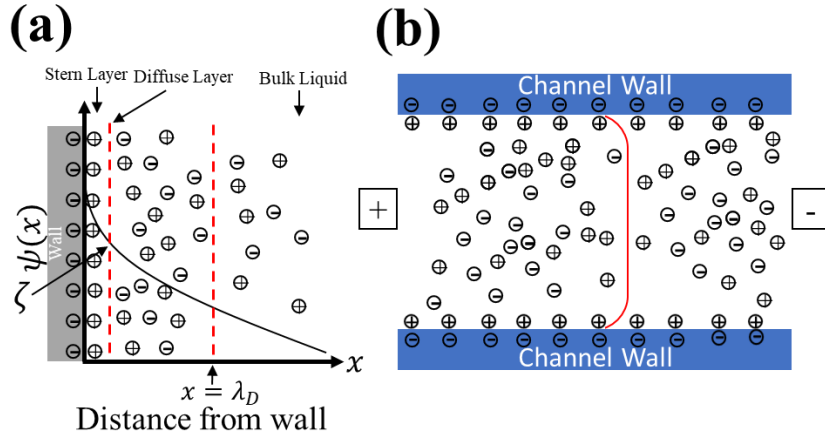


Figure 2. Schematics illustrating the electric double layer and electroosmotic flow. (a) The Stern layer is located at the interface of the PDMS wall, and the cations in the buffer are tightly bound to the charged wall. The Diffuse layer is a thicker layer with an excess of positive charges. The thickness of the electric double layer can be described by the Debye length, λ_D . The zeta potential, ζ , can be defined as the potential at the Stern layer as shown by the black arrow. The electric potential decreases linearly through the Stern layer and drops exponentially across the Diffuse layer. (b) Schematic of the electroosmotic flow velocity profile. The charge on the walls is negative, leading to the enrichment of positive charges in the associated electrical double layer. The velocity is uniform throughout the cross section and drops to zero at the liquid-solid interphase.

2.2.2. Electrophoresis

Electrophoresis refers to the motion of a charged particle in a medium by the influence of a uniform electric field.³⁰ Figure 3 represents the electrophoretic force on a charged particle. The electrophoretic force, \mathbf{F}_{EP} , on a particle with a charge q can be expressed as:³¹

$$\mathbf{F}_{EP} = q\mathbf{E} \quad (11)$$

Since the particle is moving upon the application of an electric field, the particle will experience a drag force termed Stokes drag force which is expressed as:³²

$$\mathbf{F}_d = 6\pi\eta r\mathbf{u} \quad (12)$$

where \mathbf{u} is the particle velocity and r is the radius of the particle. The EP velocity, \mathbf{v}_{EP} , can be derived when the \mathbf{F}_{EP} and the \mathbf{F}_D are balanced as follows:

$$\mathbf{v}_{EP} = \frac{qE}{6\pi\eta r} = \mu_{EP}\mathbf{E} \quad (13)$$

where q is the medium charge, η is the medium viscosity, \mathbf{E} is the electric field, and μ_{EP} is the electrophoretic mobility. The μ_{EP} can be expressed as:³¹

$$\mu_{EP} = \frac{q}{6\pi\eta r} \quad (14)$$

The μ_{EP} can also be expressed by considering that the particle radius is much larger than the double layer thickness. In this case, the electric double layer plays an essential role in controlling the electrophoretic behavior of the particle. The expression is termed the Smoluchowski's equation and is expressed as:³³

$$\mu'_{EP} = \frac{\varepsilon\varepsilon_0}{\eta}\xi \quad (15)$$

where ε_0 is the permittivity of vacuum, ε is the relative permittivity. Therefore, the electrophoretic velocity based on the Smoluchowski expression can be expressed as:³³

$$\mathbf{v}_{EP} = \frac{\varepsilon_r\varepsilon_0}{\eta}\xi\mathbf{E} = \mu'_{EP}\mathbf{E}\xi \quad (16)$$

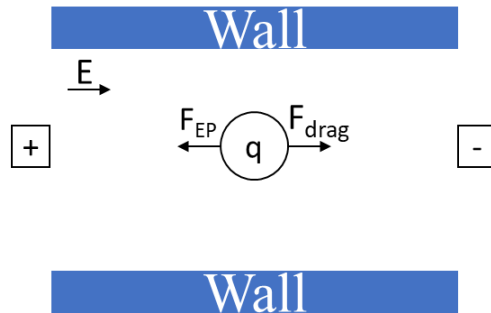


Figure 3. Schematic of an electrophoretic force acting on a particle.

2.2.3. Dielectrophoresis

Dielectrophoresis refers to the migration phenomenon when a polarizable particle is subjected to a nonuniform electric field. In a microfluidic device, the nonuniform electric field can be generated by insulating posts or structures in the fluidic channel. The DEP force acting on a spherical particle can be expressed as:³⁴

$$\mathbf{F}_{DEP} = 2\pi r^3 \epsilon_m \text{Re}[f_{CM}(\omega)] \nabla E^2 \quad (17)$$

where $\text{Re}[f_{CM}(\omega)]$ is the Clausius-Mossotti (CM) factor. The CM factor at low frequencies (<50 kHz) is described as:³⁵

$$\text{Re}[f_{CM}(\omega)] = \left(\frac{\sigma_p - \sigma_m}{\sigma_p + 2\sigma_m} \right) \quad (18)$$

where σ_p and σ_m are the conductivities of the particle and medium, respectively. The CM factor dictates the migration of the particle in a nonuniform electric field. If the particle conductivity is lower than the conductivity of the medium ($\text{Re}[f_{CM}(\omega)] < 0$), then the particle migrates towards small electric field regions, termed negative DEP. On the other hand, if the conductivity of the particle is greater than the conductivity of the medium ($\text{Re}[f_{CM}(\omega)] > 0$) then the particle migrates to the high electric field region and is termed positive DEP.

CHAPTER 3

A CONTINUOUS HIGH-THROUGHPUT INSULATOR-BASED DIELECTROPHORESIS DEVICE FOR SIZE-BASED PARTICLE SEPARATION

3.1. Introduction

Resolving the subpopulations of organelles is important as size-heterogeneity in organelles has been linked to specific diseases such as neurodegenerative diseases,³⁶ cardiovascular diseases,³⁷ infectious diseases,³⁸ and cancer.³⁹ One of the most vital organelles with a significant contribution to any cellular functions is mitochondrion. Mitochondria size and morphology is regulated by fusion and fission processes in response to the cell environment.^{40, 41} Distributions of normally sized mitochondria average ~600 nm, while abnormally large mitochondria are typically $>1 \mu\text{m}$ and small mitochondria $<300 \text{ nm}$.^{42, 43} Abnormally large mitochondria have been linked to diseases such as Parkinson disease,¹⁷ acute lymphocytic leukemia,⁴⁴ and microvascular alterations in renal allografts.⁴⁵ Fractionating mitochondria populations by size could thus provide an important tool to assess the biomolecular differences in organelle subpopulations.

Different separation techniques have been developed to fractionate mitochondria by size. Centrifugation techniques such as differential centrifugation^{44, 45} and density gradient centrifugation⁴⁵⁻⁴⁸ and chromatographic techniques such as liquid chromatography⁴⁹ are the major extraction methods to separate organelles in fractions. Electrokinetic (EK) techniques such as free-flow fractionation⁵⁰ and capillary electrophoresis⁵¹ were developed to alleviate sample contamination (e.g., lysosomes) during centrifugation. An effective tool that has been recently exploited for the separation of biomolecules is dielectrophoresis (DEP). Since the DEP force scales with the radius of

the particle to the third power and the electric field gradient (see equation 17), this method has been applied to different analytes of interest ranging from nanometer to micron scale.^{26, 52} For example, the separation of bacteria,⁵³⁻⁵⁵ DNA,⁵⁶⁻⁵⁹ proteins,⁶⁰⁻⁶³ and carbon nanotubes⁶⁴⁻⁶⁶ has been reported in insulator-based dielectrophoresis (iDEP) devices.

Achieving high-throughput separation is required to recover ample sample for analysis to elucidate the role that organelle heterogeneity plays in human biology and diseases. Different DEP-based microfluidic devices have been developed previously for high-throughput separation. Wu et al. developed a microfluidic platform coupled with DEP to separate yeast cells and polystyrene beads with a recovery efficiency larger than 90%.⁶⁷ High-throughput was also achieved by microfabricating 3D electrodes in a microfluidic device.⁶⁸ This microfluidic platform was able to separate 10^6 cells/min at flow rates of $10 \mu\text{L}/\text{min}$. Dielectrophoresis has also been combined with other separation techniques for high-throughput separation. For example, Jiang et al. developed a microfluidic device that combined hydrophoretic and dielectrophoresis to separate neural stem cells.⁶⁹ This device achieved a throughput of 2.4×10^5 cells/h at $3.5 \mu\text{L}/\text{min}$. A drawback of these devices is that microfabrication is more cumbersome and resource-intensive since electrodes need to be microfabricated in the microfluidic.

Recently, ratchet migration has been demonstrated to be a good candidate for the separation of mitochondria. In this migration mechanism, a periodic potential is applied to an asymmetrical post geometry to induce separation. Such approach has been demonstrated for sorting and separating different particle sizes.^{20, 21, 70} In the past, we designed a ratchet device capable of separating particles in a sub-micrometer regime. We

demonstrated the separation of 0.28 and 0.87 μm polystyrene beads, mitochondria, and liposomes using this ratchet migration.²² The separation was achieved by applying a complex waveform that introduced electrokinetic and dielectrophoretic forces to induce a migration mechanism that differs based on the size of the particles.

Here, a microfluidic device for the separation of polystyrene particles under a continuous flow is presented. The particles are separated by a migration mechanism that induces electrokinetic and dielectrophoretic forces on the particles simultaneously. The particle migration was assessed by calculating the migration velocities of the particles. This device offers the ability of size-tuning by simply modifying the electrical parameters and takes advantage of steering particles into opposite directions with similar electrokinetic parameters. Furthermore, different HT ratchet device designs are presented to demonstrate the ratchet mechanism on a large scale.

3.2. Experimental Details

3.2.1. Materials and Chemicals

Fluorescently-labeled polystyrene beads, size of 0.28 μm (FP0262-2) and 0.87 μm diameters (FP-0852-2), were purchased from Spherotech (Lake Forest, IL, USA). Polydimethylsiloxane (PDMS, SYLGARD 184 silicone elastomer kit) was purchased from Dow Corning Corp (Midland, MI, USA). 4-(2-Hydroxyethyl)- piperazine-1-ethanesulfonic acid (HEPES), poly(ethylene glycol)-block-poly(propylene glycol)-block-poly(ethylene glycol) (Pluronic F108), potassium hydroxide (KOH), and sucrose were purchased from Sigma-Aldrich (St. Louis, MO, USA). Pure deionized (DI) water was collected from an Elga water purification system (Woodridge, USA). Microscope glass

slides (75 mm × 25 mm × 1.0 mm) were purchased from Thermo Fisher Scientific Inc. (Waltham, MA, USA). Platinum wire (0.3 mm) was purchased from Alfa Aesar (Ward Hill, MA, USA).

3.2.2. Sample Preparation

A 10 mM HEPES buffer solution containing 250 mM of sucrose and 1 mM of F108 was prepared. The pH was adjusted to 7.4 by 1 M of KOH (the conductivity of the solution was 0.03 S/m) and the buffer solution was filtered by a 0.2 μm filter. A suspension polystyrene beads containing 0.1 % w/v of 0.87 μm and 0.03 % w/v 0.28 μm polystyrene beads was prepared as described below. The bead suspension was resuspended by 10 s vortexing. Finally, the bead suspension was diluted with the buffer solution by a dilution factor of 30, and the bead suspension was incubated overnight to ensure F108 coating on the particles.

3.2.3. Device Fabrication

The microfluidic device was designed via AutoCad (Ver. 2018, AutoDesk, Mill Valley, CA, USA), and the photo-mask was purchased through Advance Reproduction Corp. (North Andover, MA, USA). Next, the master mold was fabricated by a standard photolithographic process using a negative photoresist. Briefly, on a 4" silicon wafer (University Wafer, South Boston, MA, USA), a 15 μm thick layer of photoresist (SU-8 2020, Sigma-Aldrich, St. Louis, MO, USA) was spin-coated, which was then exposed to UV light through the photo-mask using a Suss MJB4 Mask Aligner (Suss MicroTech, Germany). After exposure, the photoresist was developed using SU-8 developer (Kayaku Advanced Materials, Westborough, MA, USA) and baked at 150 °C for 30 min

prior to use.

The PDMS was prepared by mixing base prepolymer and curing agent at a ratio of 10:1 (w/w ratio, base prepolymer: curing agent), which was poured on the master mold. Then, the PDMS was degassed using a desiccator and cured in an oven at 70 °C overnight. Next, the cured PDMS was peeled off from the master mold, and 3 holes for the reservoirs were punched using Biopsy punches (Henry Schein, Phoenix, AZ, USA), one for inlet (1.5 mm), and the other two for outlets (3 mm). The imprinted PDMS was cleaned with isopropanol (IPA) and dried in an oven at 70 °C overnight. The cleaned PDMS piece and a glass slide (25mm x 75mm x 1mm) were bonded by treatment with oxygen plasma using a plasma cleaner (PDC-001; Harrick Plasma, Ithaca, NY, USA). Then, the channel was coated with the 1mM F108 mixed in the buffer solution, and the devices were sealed and stored in 100% humidity conditions prior to be used for experiments.

3.2.4. Device Set-up

The common inlet was connected to a 50 μ L syringe (Hamilton, NV, USA) via a silica capillary (Molex, Phoenix, AZ, USA), and the sample was injected into the device using a syringe pump (Harvard Apparatus, MA, USA) at 20 nL/min. A platinum electrode was inserted in each outlet and one electrode was connected to the ground, and another was connected to high-voltage equipment (AMT-3B20, Matsusada Precision Inc., Japan), which applies the potential difference using micro-clamp (LabSmith, Livermore, CA, USA). Additionally, in each outlet reservoir, 10 μ L buffer solution was added, and 5 μ L of mineral oil was applied on top of the buffer solution to prevent the drying of outlets

due to evaporation of the buffer solution during the experiment.

3.2.5. Detection and Data Analysis

Fluorescence images were obtained using an inverted microscope (IX71, Olympus, Center Valley, PA, USA) equipped with a 100 W mercury burner (URFL-T, Olympus) with 40× (NA = 0.60) objective, an Optosplit element (Oxford Instruments, UK), and multiband fluorescence filter set (exciter Brighline 468-553, dichroic FF493/574-Di-01, emitter Brightline 512-630, Semrock, USA). Videos were recorded by a CCD camera (QuantEM:512SC, Photometrics, Tucson, AZ, USA) using Micro-Manager software (version 1.4.7, Vale Lab, UCSF, CA, USA). The Optosplit enabled recording fluorescence signals of two different wavelengths simultaneously. The recorded videos were processed by ImageJ software⁷¹ (version 1.53, NIH) and Mosaic particle tracker plugin⁷² was used to trace the particle migration. The experiment was repeated three times, and at least 40 particles were tracked. Then, the migration velocity of particles was calculated by an in-house script written in MATLAB (R2020, MA, USA).

3.3. Results and Discussion

3.3.1. Working Principle of Migration Mechanism

We designed a continuous flow separation microfluidic device combining the action of electrokinetic, dielectrophoretic, and hydrodynamic flow. The microfluidic device (Figure 4a) contained a periodic array of insulating microposts (Figure 4b) similar to a previously reported ratchet device.²² However, particles were introduced into the post array region via two inlets employing continuous pressure-driven flow (PDF). In addition to the PDF, the applied periodic waveform (see Figure 4c) induced electrokinetic

migration and DEP. Large particles experiencing nDEP were trapped at the flat surface of the microposts where the electric field was weakest (Figure 4d), on the contrary, smaller particles were not trapped because they were not experiencing sufficient nDEP. This ratchet separation principle was overlaid here with the PDF component, and we investigated suitable parameters for particle separation by size in continuous mode.

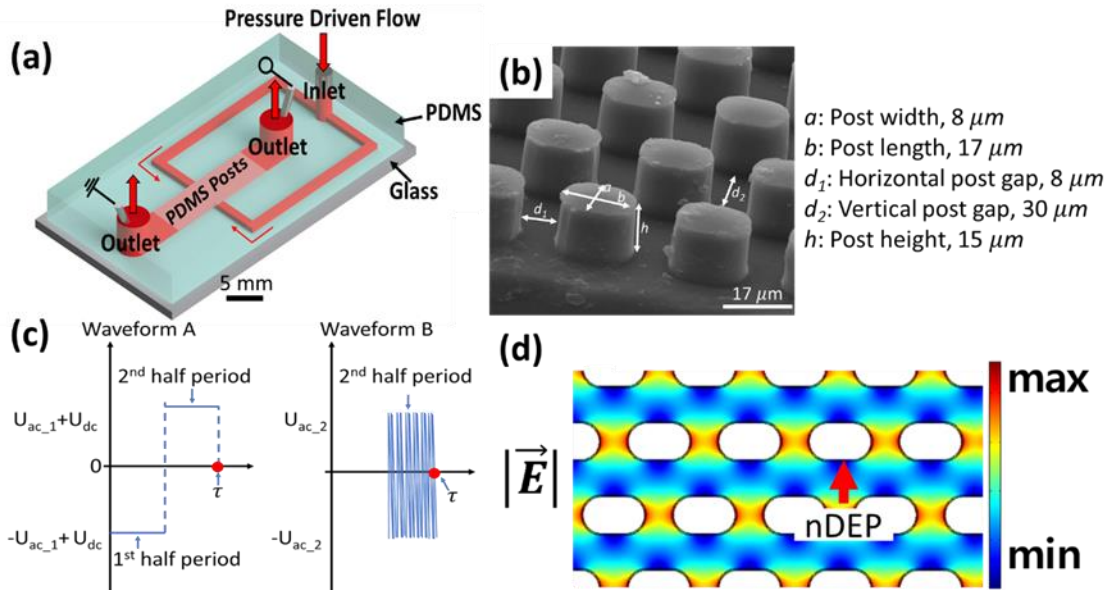


Figure 4. (a) Schematic of the ratchet device. The device has an inlet and two outlets for sample collection. Platinum wires were installed in each outlet. The distance between the two outlets was 1 cm, the width of the channel is 2 mm, and the main channel contains an array of insulating posts. (b) SEM image shows the insulating posts in the main channel. The dimensions of the well-resolved posts are summarized next to the SEM image. (c) Waveforms applied for the electrokinetic components inducing ratchet migration. Waveform A switch applies $\pm U_{ac_1}$ with a DC potential offset, U_{dc} (here for $U_{dc} > 0$). Waveform B is a sinusoidal signal applied in every second half of the driving period of U_{ac_1} at 10 kHz. T indicates the length of one complete driving period. (d) Electric field distribution obtained from the COMSOL model. The arrow points to the regions of low electric fields, where nDEP occurs for polystyrene beads and mitochondria.

In Figure 5a-g, the working principle of the ratchet migration mechanism is explained based on the case of PS particles. During ratchet migration, the large particles experienced ratchet migration (assigned negative sign for migration velocity) and the smaller particles experienced normal migration (assigned positive sign for migration velocity) when subjected to the periodic driving force. This effect was induced by a periodic electrical driving force U_{ac_1} with defined U_{dc} offset, coupled to a higher frequency component in the second half period (U_{ac_2}), see Figure 4c, to induce DEP trapping and the migration direction reversal for large particles. Overlaid with the PDF component, the various forces on the particles were schematically outlined in Figure 5a-b in the two half-driving periods. While the PDF component was the same in each driving period, the switch of the sign in the electrical potential in the second half period reverses the electrokinetic driving forces. The EK force resulted from the sum of electroosmotic and electrophoretic contributions.

In combination with the PDF, the migration directions of two differently sized particles can now be described for each half driving period (Figure 5c-f). We first discuss the situation in the top section of the device (Figure 5c-d). In the first half-driving period, since EOF was the stronger force dominating the EK migration direction, the net direction of the small and large particle migration was toward the top outlet. PDF accelerates the migration of both particles toward the top outlet because the direction of PDF and EOF components were the same (Figure 5c). As the DEP force was generated in the second half driving period, the large particles were trapped at the insulating posts. However, the strength of DEP on the small particles was not sufficient to induce trapping, thus, the small particles traveled toward the bottom outlet. PDF decelerates the migration

of small particles because the migration direction is opposite to the overall electrokinetic contribution, but the strength of PDF was weaker than that of the EK force (Figure 5d). Overall, the migration of the large particles in the top section resulted in migration towards the top outlet, whereas the migration of the small particles resulted in the opposite direction.

In the bottom section of the device (Figure 5e-f), PDF and overall EK migration direction were opposite in the first half-driving period. As a result, both particles were migrating toward the top outlet (Figure 5e). In the second half driving period, the large particles were trapped at the microposts due to nDEP, and the small particles were migrating toward the bottom outlet because the overall EK migration and PDF were in the same direction (Figure 5g). The migration direction of the small particles was denoted as normal migration because the small particles were not affected by the ratchet migration. In conclusion, the magnitude of the resulting migration velocities strongly depends on the interplay of PDF with EK components.

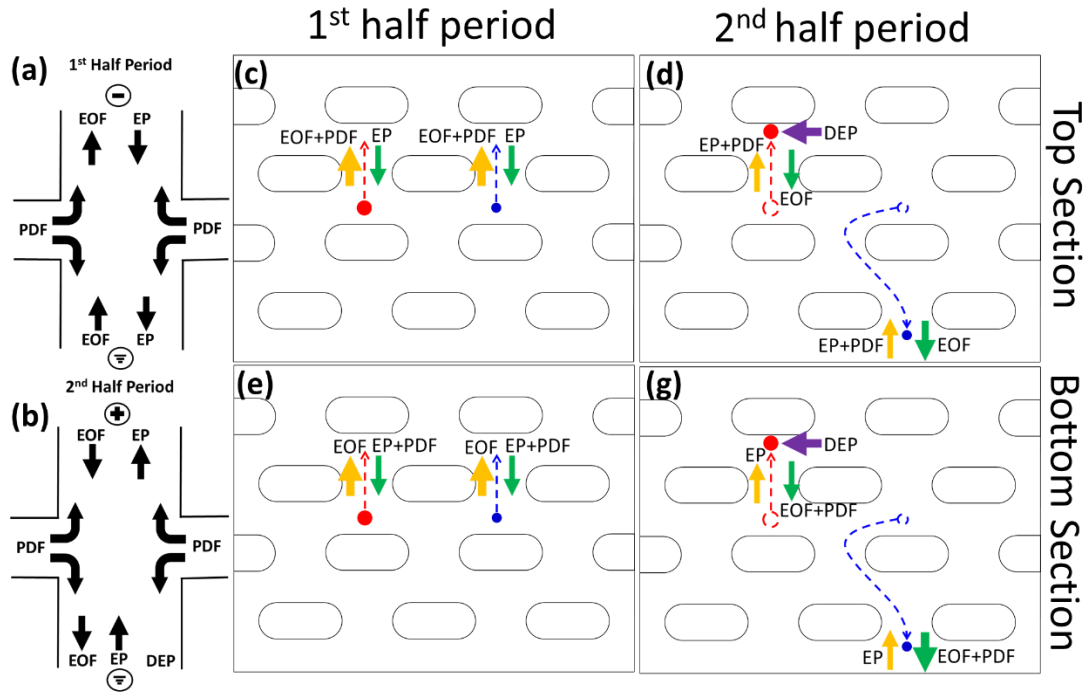


Figure 5. (a-g) Illustration of forces and the migration direction they induce during the first (a) and second half driving period (b). (c-g) Exemplary particle trajectories in the two sections of the device. (c-d) top section and illustration of the particle migration in the first (c) and second (d) half driving period. Dashed lines indicate particle trajectories, and arrows indicate the direction migration based on the respective force. In the first half period of waveform A, both particles migrate towards the top electrode since the EOF and PDF overcome the EP force. In the second half driving period, waveform B is superimposed on waveform A. In this case, the large particle is trapped by the DEP force, and the small particle migrates towards the bottom section of the device. (e-g) On the bottom section of the device, the two particles migrate towards the top section of the device since the EOF is overcoming EP and PDF in the first half driving period. In the second half driving period, the large particles are trapped by DEP, and the small particles migrate towards the bottom, overcoming EP forces.

3.3.2. Experimental Observation of Migration Mechanism with Model Beads

The polystyrene beads migration velocities were assessed from a numerical model (not on thesis) and compared to experimentally obtained particle migration under identical driving conditions. Figure 6 compared the average velocities for $0.28 \mu\text{m}$ and $0.87 \mu\text{m}$ polystyrene beads as assessed through particle tracking. The velocities were

studied for U_{ac_1} amplitude from 70 V to 90 V and varying DC offsets ($U_{dc}=10-30$ V). Figure 6a-c show the average velocity of large particles assessed in the top section of the device. Negative velocities were apparent for the large particles indicating ratchet migration. The numerical model supports the ratchet migration of the large particles on the top section of the device in good agreement with experimental migration velocities showing similar trends. It is noted that the increase of U_{ac_1} had a negligible effect on the migration velocity for the $0.87 \mu\text{m}$ particles, presumably due to a negligible increase of only 20 V. However, the increase in U_{dc} decreases the amplitude and decelerates the migration of the particles towards the top outlet of the device. This trend is apparent in the model and experiment.

Figure 6d-f show the average velocities of the smaller $0.28 \mu\text{m}$ PS beads at different U_{ac_1} and U_{dc} assessed on the bottom section of the device. Similar trends in the variation of U_{dc} are also apparent in model and experiment. In contrast to the large beads in the top section, the migration velocities now increase with increasing U_{dc} . This behavior is caused by the PDF accelerating the normal EK migration direction in the bottom region of the device. In addition, the average velocities at $U_{ac_1}=70$ V showed excellent agreement with the numerical model, whereas the experimental values at $U_{ac_1} = 80-90$ V deviated slightly from the numerical model. The discrepancy between the model and experiment for the demonstrated conditions are attributed to deviations in the magnitude of the PDF in experiments, where over the course of the experiment might have deviated from 20 nL/min due to evaporation effects and fluctuations in the applied flow rates.

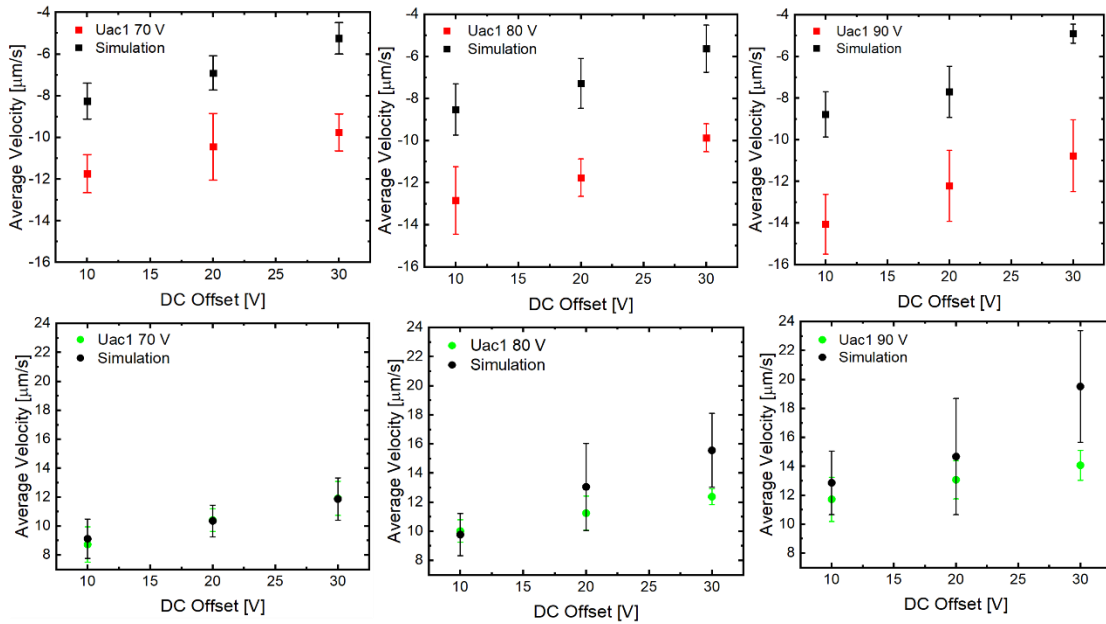


Figure 6. Average velocities of 0.28 and 0.87 μm diameter polystyrene beads investigated experimentally and as obtained from the numerical model. (a-c) large particles assessed in the top portion of the device: (a) velocities assessed at $U_{ac_1} = 70$ V, U_{dc} varying from 10 to 30 V, (b) velocities assessed at $U_{ac_1} = 80$ V, U_{dc} varying from 10 to 30 V, (c) velocities assessed at $U_{ac_1} = 90$ V, U_{dc} varying from 10 to 30 V. (d-f) small particles assessed in the bottom portion of the device: (d-f) same conditions as (a-c). For all conditions, U_{ac_2} was 1200 V at 10 kHz and the driving period 10 s. At least 40 particles were traced in each case. Note that velocities for the large particles exhibit negative signs corresponding to ratchet-based migration and small particles exhibit positive velocities. The opposing sign also indicated opposing migration directions and thus separation of the two particle species. The error bars indicate the standard deviation of average velocity obtained at each U_{dc} by tracking at least 40 particles. Three devices were used.

3.3.4. New Microfluidic Devices for High-Throughput Separation

High throughput for the separation of organelles is ideal for biomolecular assessment. In this section, three devices were redesigned from our previous geometries.⁷³ The contactless device (Figure 7a-c) has a PDMS barrier that separates the electrode channel (filled with gallium) and the fluidic channel. This design was elaborated to avoid exposing the sample directly to the electrode as well as to collect the

heterogeneous sample from the two outlets (Figure 7d-e). The first device is a larger scale to the device shown in Figure 4a. The device keeps the same outlet scale; however, in one design, it adds a gradient next to the channel. The contact device (Figure 7f-h) has a larger post array (5 mm in width and 1 cm in length) than the other two devices. In this device, an electrode channel is introduced to create an electric field in the ratchet area. The electrode channel is filled with liquid gallium and stops at the barrier post due to the viscosity of the gallium. Furthermore, this device has three outlets that will be used to collect heterogeneous sample, and the third outlet will be used as a waste outlet.

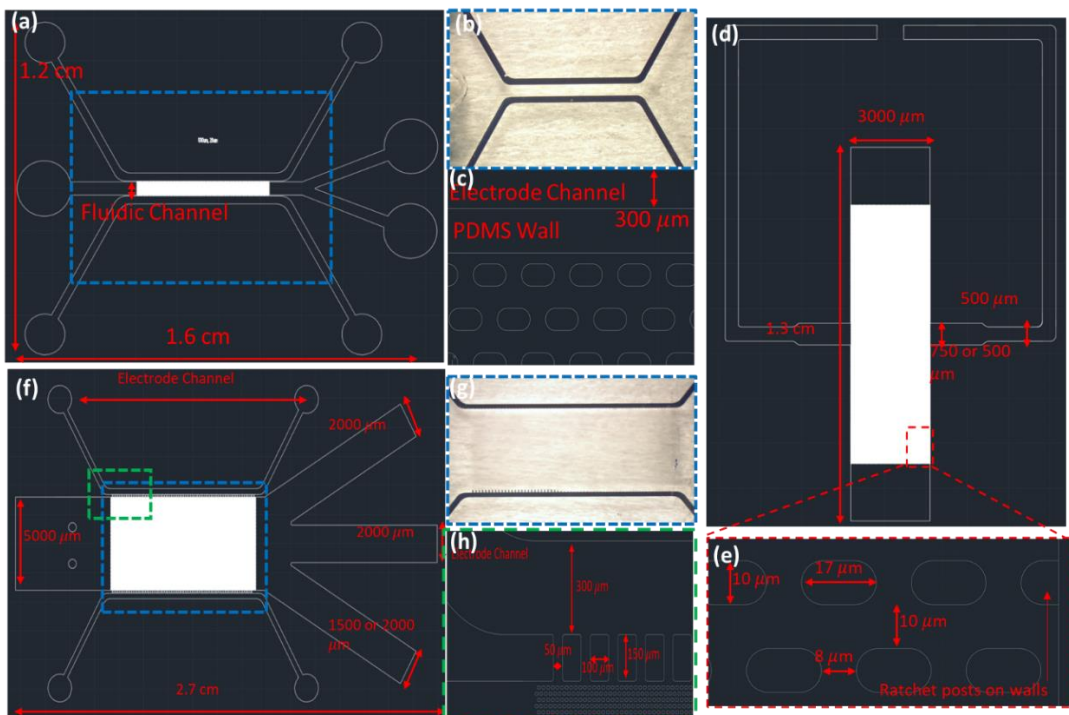


Figure 7. Schematic overview of the contact, contactless, and continuous devices and optical images of injected gallium. (a) Schematic overview of the contactless device. (b) Optical image of the injected gallium. (c) Zoom image into the electrode channel, PDMS wall, and ratchet area (d) Schematic overview of the continuous device. (e) Zoom image into the ratchet area. (f) Schematic overview of the contact device. (g) Optical image of the injected gallium. (h) Zoom image into the electrode channel, barrier post, and ratchet area.

3.4. Conclusion and Future Direction

Various HT devices were designed and fabricated for high-throughput separation. In this work, 0.87 and 0.28 μm polystyrene beads were manipulated by applying a complex waveform. Here, the larger particles demonstrated ratchet migration (negative migration), and the small particles demonstrated normal migration (positive migration). In addition, various HT devices were designed to be applied for HT separation. The contactless and contact devices were successfully filled with gallium, indicating that the geometry was not faulty. In the future, these devices will be tested using polystyrene beads and finding the experimental conditions for high throughput. In addition, numerical models will be developed for each device to aid in the experimental parameters.

CHAPTER 4

A TUNABLE INSULATOR-BASED DIELECTROPHORESIS SYSTEM FOR THE SEPARATION OF PARTICLES

4.1. Introduction

Insulator-based dielectrophoresis (iDEP) has been used for the manipulation of many analytes.⁷⁴ These devices typically employed insulating constrictions, post arrays, or other geometrical features to induce a nonuniform electric field to manipulate various analytes. However, when scaling down to biomolecules, challenges arise in manipulating particles by dielectrophoresis. The main challenges emerge since the DEP force scales with the particle radius and polarization properties (see equation 17) of the particle. Hence, nm size particles and low polarizable particles exhibit low DEP force. Therefore, to generate high electric fields, one needs to apply large electric potentials or microfabricate nanoconstrictions.¹⁴ However, large potentials can cause Joule heating,^{75, 76} and fabricating nanoconstrictions can be time-consuming and expensive.⁵⁷

Nevertheless, biomolecules have been manipulated by DEP even though the theoretical background is not well understood. For example, DNA molecules of different sizes have been manipulated by a nanopipette,^{77, 78} silicon nanotweezers,^{79, 80} and insulating constrictions.^{12, 56-58, 81, 82} In addition, proteins have also been manipulated by nanopipettes⁸³ and insulating barriers.^{61-63, 84-86} However, these demonstrations required frequencies magnitudes in the MHz range and media conductivity in the order of 10^6 $\mu\text{S}/\text{cm}$. The application of these frequencies can induce Joule heating⁸⁷ and sample deterioration.^{88, 89} In addition, high conductivity buffers can change the morphology of biological samples.⁹⁰⁻⁹² To alleviate the issue of large potentials to invoke high electric

fields, a normally-closed valve was microfabricated to act as an insulating constriction when a potential is applied to fine-tune the electric field gradient.

Microvalves have been used in different microfluidic applications such as cell sorting⁹³ and on-chip chemical synthesis.⁹⁴ Typical microvalves can be actuated electrokinetically,⁹⁵⁻⁹⁷ mechanically,⁹⁸⁻¹⁰⁰ and pneumatically.^{101, 102} Interesting applications such as pre-concentration of DNA¹⁶ and peptide sample injection¹⁰³ have been demonstrated using a pneumatic valve in a microfluidic device. In addition, pneumatic valves have been used to generate nanoconstrictions by pushing down the valve for preconcentration and trapping of analytes.^{15, 16} In the past, we designed a normally-open valve that acted as an insulating constriction when deflected into the channel for the tunability of the electric field gradient to manipulate polystyrene beads and DNA.¹⁰⁴ Here, we further optimize the valve by designing a normally-closed valve to fine-tune the electric field and valve actuation.

In normally-closed valves, the membrane is actuated by application of a vacuum to the control channel.¹⁰⁵ This type of valve has been extensively used for active mixing from a standard solution with a sample^{106, 107} and fluid control.¹⁰⁸ Here, a normally-closed valve is microfabricated in the microfluidic device that acts as a dynamic insulating constriction when a potential is applied across the channel. The tunability of the electric field gradient is investigated by building a numerical model. The regulation of the valve was investigated by a pressure study. Finally, a proof of principle experiment was realized by manipulating 0.87 μm polystyrene beads by fine-tuning the electric field gradient changing the deflection of the valve.

4.2. Experimental Section

4.2.1. Material and Chemicals

The 0.87 μm polystyrene beads (FP-0852-2) were purchased from Spherotech (Lake Forest, IL, USA). The fluorescein sodium salt were purchased from Sigma-Aldrich (St. Louis, MO, USA). The chemicals to prepared the buffer solution were the same as in chapter 3. The microscope glass slides and platinum wires were also the same as in chapter 3.

4.2.2. Microchip Fabrication

Two silicon master wafers were fabricated by photolithography. For the control layer, a 6:1 w/w ratio of PDMS to curing agent was prepared and poured onto the silicon wafer. For the fluid layer, a 15:1 w/w of PDMS to curing agent poured onto the wafer and spin coated (30 s at 1900 rpm) to yield a thickness of 20 μm . The control and fluidic layers were put in the oven for 30 min at ~ 70 C to semi-cured the PDMS. After 30 min, the control layer was peeled off from the wafer, and the vacuum valves were punched with a 1 mm Biopsy punch (Henry Schein, Phoenix, AZ, USA), and the control layer was manually aligned on the fluidic layer using a stereomicroscope. Figure 8 shows a schematic representation of the assembled microfluidic device. The dimensions of the control channel and valves are summarized in Table 1. After alignment, the PDMS control and fluidic layer were put back in the oven overnight to fully cure the PDMS. After curing, the PDMS was peeled off from the silicon wafer, cleaned with IPA, and blow-dried with nitrogen gas. The PDMS slab and glass slide were put in the oxygen plasma (PDC-001; Harrick Plasma, Ithaca, NY, USA) and exposed for 1 min at high

frequency setting. After plasma exposure, the PDMS and glass slide were placed in the oven at 70 °C for 20 min. After 20 min, the PDMS and glass slide were bonded together and filled with the HEPES buffer solution containing sucrose and F108. After filling the device, the device was stored in a humid environment.

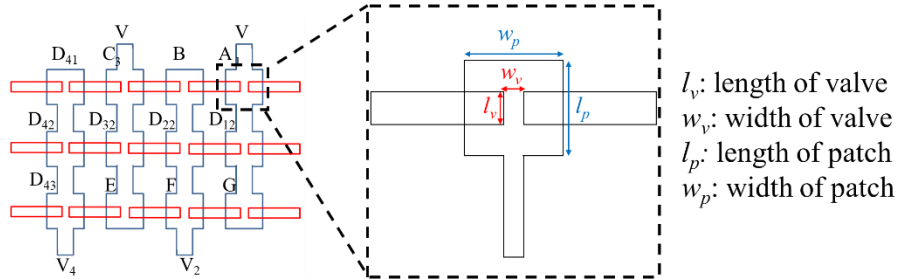


Table 1. Dimensions of stem valve and valve patch.

| Valve Location [μm] | A | B | C | D | E | F | G |
|-------------------------------------|-----|-----|-----|-----|-----|-----|-----|
| w_v | 100 | 75 | 50 | 25 | 20 | 15 | 10 |
| w_p | 400 | 300 | 250 | 250 | 250 | 250 | 250 |
| l_p | 400 | 300 | 250 | 250 | 250 | 250 | 250 |
| l_v | 100 | 100 | 100 | 100 | 100 | 100 | 100 |

Figure 8. Schematic representation of the top view of assembled microfluidic. The zoom-in image shows one section of the valve assembled. Table 1 shows the dimensions of the control channel and the fluidic channel.

4.2.3. Sample Preparation

A 10 mM HEPES buffer solution containing 250 mM of sucrose and 1 mM of F108 was prepared. The pH was adjusted to 7.4 by 1 M of KOH (the conductivity of the solution was 0.03 S/m), and the buffer solution was filtered by a 0.2 μm filter. A suspension of polystyrene beads containing 0.1 % w/v of 0.87 μm was prepared. The bead suspension was resuspended by 10 s vortex. Finally, the bead suspension was diluted with the buffer solution by a dilution factor of 30, and the bead suspension was

left overnight to ensure F108 coating on the particles.

4.2.4. Device Set-up

The vacuum line, connected to the control channel, was connected using stainless-steel pins (2 cm, IDEX Corporation, USA). A MFCS-EZ system (Fluigent, France) was used to induce vacuum. The MFCS-EZ was controlled by the Fluigent software. Platinum electrodes were connected on the two outlets and attached by micro-clamps to a high voltage amplifier (AMT-3B20, Matsusada Precision Inc.) driven through a Multifunction DAQ card (USB X Series, National Instruments, TX, USA) programmed by LabVIEW 2014 (version 14.0, National Instruments).

4.2.5. Detection and Data Analysis

Fluorescence images were acquired with an inverted microscope (IX71, Olympus, Center Valley, PA, USA) equipped with a 100 W mercury burner (U-RFL-T, Olympus, Center Valley, PA, 54 USA) and a fluorescence filter set (0.87 μ m beads: exciter ET470/40, dichroic T495LP, emitter ET525/50, Semrock, USA). Images and videos were captured by a CCD camera (QuantEM:512SC, Photometrics, Tucson, AZ, USA) and Micro-Manager software (version 1.4.7, Vale Lab, UCSF, CA, USA). The obtained videos were processed by ImageJ software. The fluorescence intensities of the actuated valves and channels heights were measured by ImageJ.⁷¹

4.2.6. Numerical Modeling

A numerical model was constructed using COMSOL Multiphysics 5.4. Briefly, a geometry of an actuated valve was drawn in COMSOL. To solve the electric field gradients, the Electric Current module was used. The detailed parameters for the numerical model are summarized in Appendix A.

4.3. Results and Discussion

4.3.1. Numerical Model Results

The changes in the electric field gradient were simulated using COMSOL Multiphysics. Figure 9a shows the geometry used in the COMSOL model. The gap distance from the valve to the glass substrate (d_{gap}) was changed from 0.1-10 μm , and the simulation was run for each d_{gap} (0.1-10 μm). Figure 9b shows the electric field gradients for different d_{gap} at 25 V (adapted from 1000 V/cm) across the channel. The numerical model demonstrates the tunability of the electric field by reaching the necessary magnitudes to manipulate different biomolecules using the literature values.^{109, 110} For example, Swami et al.¹¹¹ manipulated single-stranded DNA (~200 bases), Sano et al.¹¹² and Camacho-Alanis et al.⁵⁷ manipulated λ -DNA (48.5 kbp) with electric field gradients with a magnitude of $\sim 10^{18} \text{ V}^2/\text{cm}^3$. The numerical model reached the same order of magnitude at 1 μm ($\sim 10^{18} \text{ V}^2/\text{cm}^3$) compared to the orders of magnitude compared above. The numerical model indicates that the electric field gradients to manipulate these biomolecules were reached at 1 μm . The gradient values can also be compared with the electric field gradient values reported to manipulate proteins. For example, the protein streptavidin has been manipulated by iDEP by different researchers by applying an

electric field gradient average of $\sim 10^{18} \text{ V}^2/\text{cm}^3$.^{84-86, 113} The experimental responses at the gradient magnitudes were in good agreement with our numerical model magnitudes at $d_{gap}=1 \mu\text{m}$. All in all, the numerical model suggests the tunability of the electric field gradients by an insulating valve. The numerical results were compared to electric field gradient values in the literature modeled to manipulate biomolecules by iDEP reaching the same electric field gradient magnitudes to manipulate the analyte.

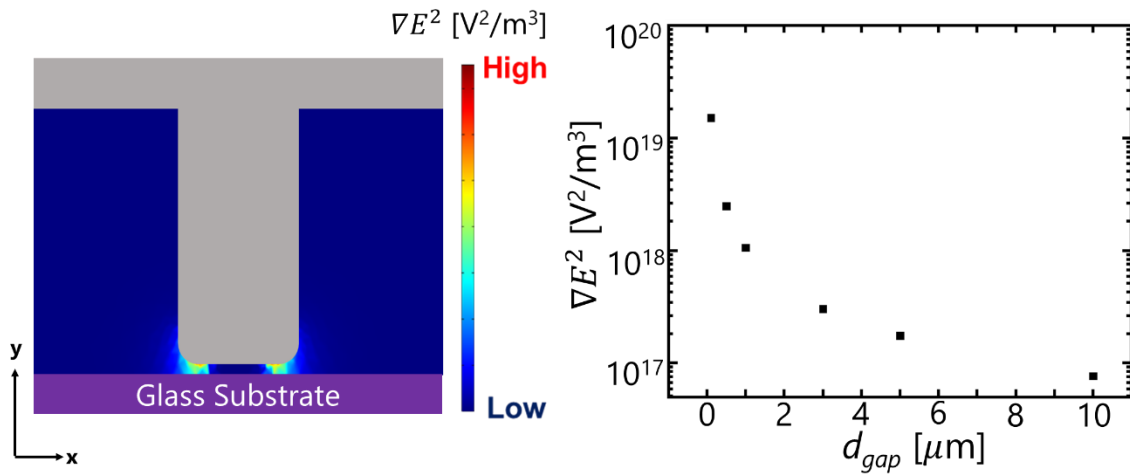


Figure 9. Schematic of COMSOL geometry and electric field values calculated from the COMSOL model. The electric field gradients were calculated by applying 1000 V/cm across the channel with a gap distance of 0.1-10 μm .

4.3.2. Operation of Dynamic Constriction and Pressure Study

A normally closed valve consists of a control and a fluidic layer (Figure 10). The control layer is attached to a vacuum system. The thin membrane lifts into the control chamber at an applied vacuum (Figure 10a). The thin membrane is comprised of a stem valve that relaxes on the glass substrate when a vacuum is not applied. When the valve is

in the closed position, the fluid is stopped by the valve (Figure 10b). When the valve is actuated, the fluid continues to flow through the fluidic channel (Figure 10c).

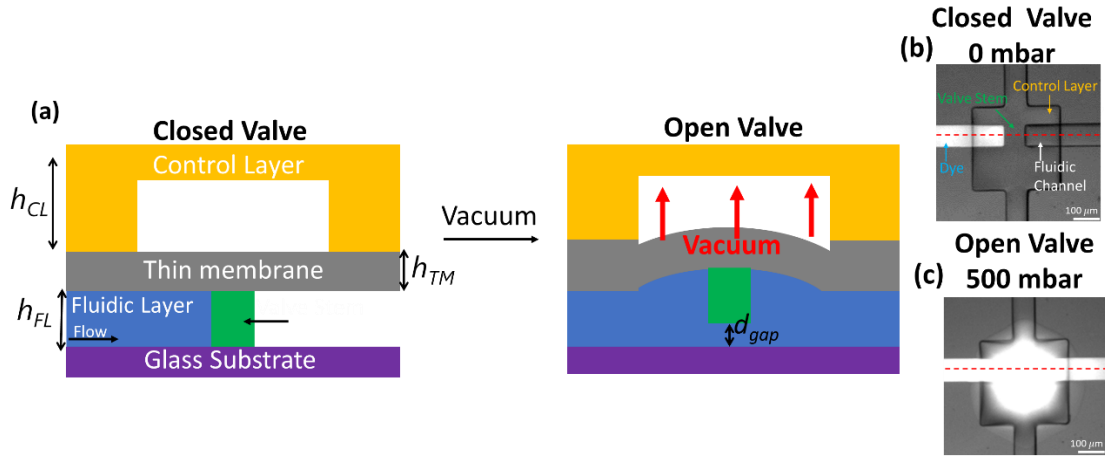


Figure 10. Schematic representation and fluorescence microscopy images of a normally closed valve in open and closed position. (a) Schematic representation of a normally-closed valve in open and closed position by an applied vacuum. The height of the control layer (h_{CL}) is 40 μm , the height of fluidic layer (h_{FL}) is 20 μm , the width of stem valve (w_v) is 10 to 100 μm , and the height of thin membrane (h_{TM})=10 μm . The cross-section of the image is indicated by the red dash line on Figures b and c. (b) Fluorescence microscopy images of a normally closed valve in closed position. The dye is stopped at the closed valve. (c) Fluorescence microscopy image of a normally closed valve in open position. The valve is actuated at 500 mbar, and the dye continuously flows throughout the microfluidic channel.

To understand the tunability of the valve, the valve pressure threshold (p_{thresh}) with respect to the aspect ratio was studied. The p_{thresh} is defined as the vacuum applied when the thin membrane touches the control layer wall. The aspect ratio, a , of each individual valve was calculated as follow:

$$\alpha = \frac{l_p w_p}{l_v w_v} \quad (18)$$

where l_p is the length of the patch, w_p is the width of the patch, l_v is the length of the valve, and w_v is the width of the valve. The p_{thresh} was experimentally determined by

applying a pressure starting at 50 mbar and increasing the pressure by 50 mbar until the actuation of the valve was visible. It was noted that a high aspect ratio requires less vacuum (200 mbar) to be actuated (Figure 11a). For example, the largest valve dimension (valve A) with an aspect ratio of 16 requires the largest vacuum (500 mbar). In addition, since the microfluidic design has multiple valves D, the pressure threshold was investigated with respect to the valve location. Figure 11b shows the pressure threshold with respect to the valve location. The p_{thresh} decreases for the D₁₂, D₂₂, and D₃₂ valve location. The valve located at D₄₁, D₄₂, and D₄₃ show similar p_{thresh} . The similar p_{thresh} for the D₄₁, D₄₂, and D₄₃ can be explained by the locations of the valves. The valves are located next to the fluidic outlets, where the extra pressure in the outlets aid in the actuation of the valves.

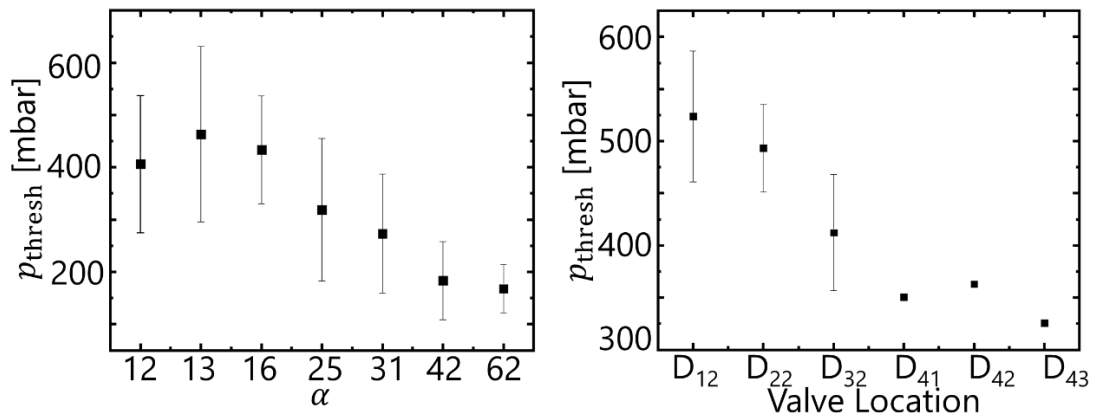


Figure 11. Pressure threshold versus aspect ratio and valve location. (a) Pressure threshold versus aspect ratio. The graph shows the pressure threshold versus aspect ratio showing that a higher aspect ratio requires less pressure for the valve to actuate. (b) Pressure threshold versus valve location. The graph shows the pressure versus valve location, indicating no correlation with the valve location. The error bars show the average p_{thresh} of three different devices. Each valve was tested at least three times.

The d_{gap} in relationship with applied pressure was assessed by examining the fluorescence intensity of an actuated valve. The distances achieved by the actuated valve were calculated from a calibration curve (Figure 12a). The calibration curve was acquired by measuring different channel heights (2, 10, 15, and 20 μm) filled with sodium fluorescein dye. Figure 12b shows the gap distances of a 25 and 75 μm width valve with respect to different vacuum pressures. The 25 μm width valve reaches a minimum distance of $\sim 10 \mu\text{m}$ at 100 mbar and a maximum distance of $\sim 25 \mu\text{m}$ at 700 mbar. The increase in d_{gap} is in accordance to our understanding of a pneumatic valve where the d_{gap} increases when vacuum applied increases. In the case of the 75 μm width valve, the d_{gap} increases at applied vacuum from 100 to 300 mbar but decreases the deflection distance after 400 mbar. This contradicts the trend observed for the 25 μm width valve. One explanation can be attributed to the malfunction of the 75 μm valve width. For example, since the dimension of the 75 μm valve are larger (valve patch: $w_v=300$ and $w_p=300$, and valve dimension: $w_v=75$ and $w_p=100$) compared to the 25 μm width valve (valve patch: $w_v=250$ and $w_p=250$, and valve dimension: $w_v=25$ and $w_p=100$) the actuation for the 25 μm valve width create less stress to the thin layer. Compared to the largest valve, where the pneumatic pressure generates more stress to the thin layer since the valve is substantially larger. Therefore, by applying this stress to the thin membrane, a rupture on the thin membrane might have happened, generating lower d_{gap} distances. In conclusion, this experiment demonstrated the fine-tuning of a 25 μm valve. However, ideally, d_{gap} in the nm regions should be achieved by the valve. This might be able to achieved by applying small vacuum magnitudes. Nevertheless, the valve geometry needs to be redesigned to achieve sub-micrometer gap distances. To measure the channel heights,

microfluidic devices with submicrometer channel heights need to be available. The resolution limit of a negative SU-8 photoresist is $\sim 1 \mu\text{m}$. However, reaching these heights might be challenging and may require fabrication optimization. 3D printing technology can also be used to print a channel height in the sub-micrometer regions since the height resolution has been demonstrated for sub-micrometer regions by this technology.¹¹⁴

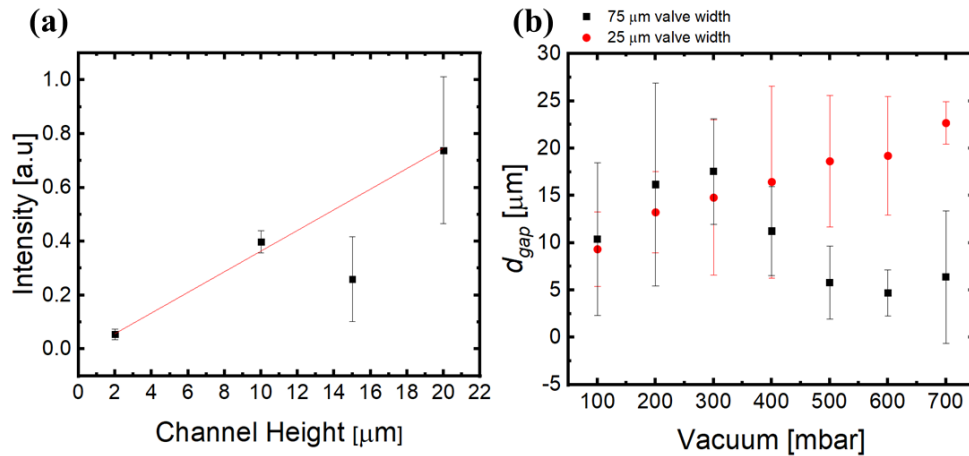


Figure 12. (a) Calibration curve acquired from the measurement of different channel heights filled with a fluorescence dye. The error bars originate from the average measurement of two devices. (b) Calculated distances from the calibration curve. Each data point represents the average value from three different devices. The errors originated from valve actuation variations. Each valve was tested three times.

4.3.3. Proof of Principle Experiment for Electric Field Gradient Tunability

As a proof of principle experiment, $0.87 \mu\text{m}$ polystyrene beads were manipulated by iDEP. The iDEP trapping behavior of the particles for various applied potentials was analyzed by measuring the fluorescence intensity in the regions near the actuating valve. The fluorescence intensity is indicative of the polystyrene beads concentration due to nDEP trapping in a small pressure-driven flow. The particles were subjected to different

potentials (100-1000 V at 10 kHz). The valves (15, 25, and 75 μm valve width) were deflected at different vacuum pressures (25, 50, and 75 mbar).

Before discussing the experimental outcomes from the study mentioned above, two experimental cases are presented in Figure 13 to discuss the experimental outcomes summarized in Figure 14. Figure 13a is representative of the case of a valve actuated by an applied vacuum of 75 mbar, and Figure 13b corresponds to the scenario where the applied vacuum is 25 mbar during the electric field application and small pressure-driven flow component. A blue dashed rectangle represents where the fluorescence intensities of the trapped particles were measured experimentally. This region was selected since it corresponds to the region of the largest electric fields. For both scenarios, the PDF is acting from the bottom to top.

Considering Figure 13a, the valve is actuated by applying 75 mbar creating a d_{gap} increasing the apparent PDF. This increment in the flow streams more particles into the fluidic channel, increasing the particle concentration in the channel. Continually, by the application of 1000 V at 10 kHz, a nonuniform electric field is generated, repelling the particles from the large electric field gradients and trapping the particles by balancing nDEP repulsion with the PDF in the opposite direction. The particle repulsion is not large enough to push back the particles from the measuring area (blue dashed rectangle).

In Figure 13b, the apparent PDF is slower compared to Figure 13a since the d_{gap} is smaller at 25 mbar. Diminishing the PDF lowers the particle concentration in the channel. In this scenario, the application of 1000 V at 10 kHz generates a higher magnitude electric field gradient since d_{gap} is smaller. Here, particles are repelled further away from the measured area (blue dashed rectangle) due to the higher electric fields. However,

some particles are still trapped (overcoming the PDF) in the measured area (Figure 13b) due to the non-uniformity of the electric field gradient perpendicular to the flow direction and due to the valve distortion during actuation.

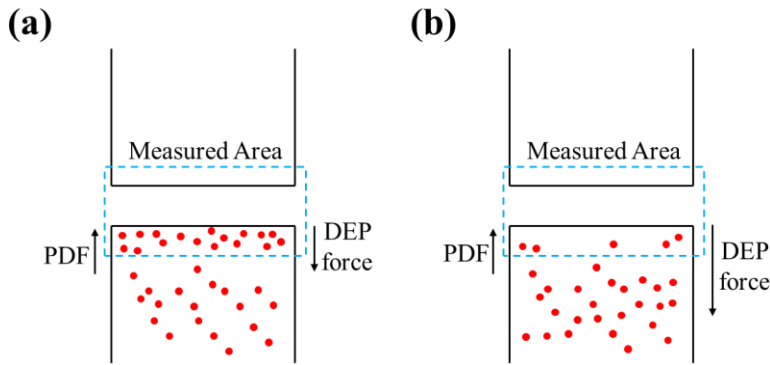


Figure 13. Schematics representing polystyrene beads subjected to different electrical parameters and valves subjected to different pneumatic pressures. A PDF is acting on the particles in addition to DEP in the direction indicated. (a) Schematic representation of trapping position for polystyrene beads subjected to 1000 V at 10 kHz. The vacuum applied is 75 mbar. (b) Schematic representation of trapping position for polystyrene beads subjected to 1000 V at 10 kHz. The vacuum applied is 25 mbar. The measured area (blue dashed rectangle) is the area selected to determine the fluorescence intensity of the particles. The pressure flow is from bottom to top. The DEP force shows the repulsion of the particles from the valve by negative DEP..

After introducing the two main experimental scenarios in Figure 13, the experimental results can now be discussed in detail. Figure 14a-c show the iDEP trapping behavior of the $0.87 \mu\text{m}$ polystyrene beads for various applied potentials (experimental conditions summarized above).

From Figure 14a-c, we can see that from 100-500 V there seems to be some or no particle trapping for each tested applied vacuum and valve. However, after gradually increasing the voltage from 600-1000 V, the $0.87 \mu\text{m}$ PS particles started to concentrate near the measured area. The gradual increase leading to particle concentration after 500 V

can be explained by the DEP force acting on the particles being large enough to start trapping the particles at 600 V.

Continually, the largest particle concentration is observed at a pneumatic pressure of 75 mbar. This was noticed for the three valves tested (15, 25, and 75 μm). On the other hand, applying a pneumatic pressure of 25 mbar resulted in less particle trapping for the three valves tested. This outcome can be explained by the different particle repulsions achieved from the created electric field gradients at the pneumatic pressures of 75 and 25 mbar. The lower pneumatic pressure (25 mbar) invokes larger electric fields (small d_{gap}), repelling the particles further away from the measured area (blue dashed rectangle), overcoming the PDF. Compared to the electric field gradient generated by the gap distance at an applied vacuum of 75 mbar, the electric field gradient is estimated to be lower due to the larger d_{gap} reached. An example of the relationship between d_{gap} and electric field gradient is summarized in Figure 9b. It is important to notice that the PDF also plays a role in the observed particle concentration since the flow rate becomes smaller at a valve actuated at 25 mbar, streaming fewer particles into the channel. On the other hand, the particle flux increases by actuating the valve at 50 and 75 mbar.

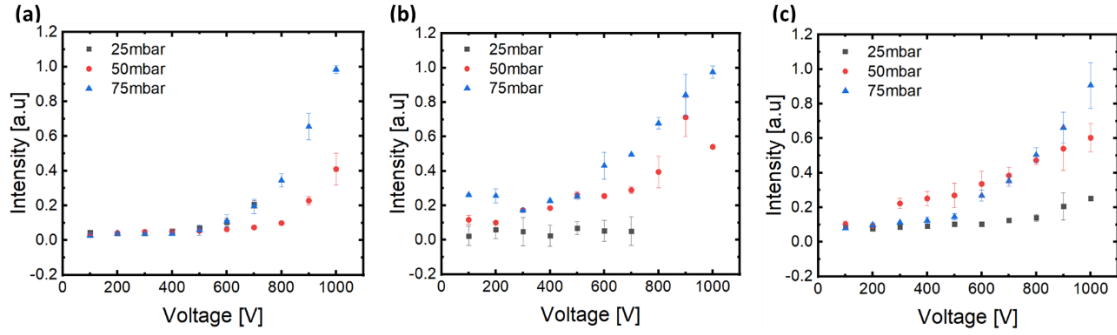


Figure 14. Fluorescence intensity variations versus different applied pressures. The intensities refer to the brightness of the polystyrene beads trapped at a selected region on the channel measured. The fluorescence intensity of the particles was measured near the perimeter of the valve. (a) The width of the stem valve is $15\ \mu\text{m}$. (b) The width of the stem valve is $25\ \mu\text{m}$. (c) The width of the stem valve is $75\ \mu\text{m}$. The error bars are the average intensity measurements of two different devices. The valve was actuated three times.

4.4. Conclusion and Future Work

A microfluidic device with a normally closed valve was presented for the fine-tuning of the electric field gradient. The valve tunability was demonstrated by a numerical model indicating that at lower d_{gap} the electric field increases. The numerical model results were compared to different electric field gradient models from the literature to manipulate bioanalytes. In addition, a pressure study was realized to understand the tunability of the valve with respect to the vacuum applied to the system. Finally, a proof of principle experiment demonstrated the fine-tuning of the electric field gradients to manipulate polystyrene beads by nDEP.

In the future, more experiments need to be developed to test the separation capabilities of this microfluidic device. Furthermore, new microfluidic devices can be designed by applying the pressure studies presented in this chapter. Finally, further studies need to be conducted to reach the nm gap distance when actuating the valve.

Reaching nm gap distances on demand will be crucial for separation science since one microfluidic device will be tunable for different analytes. The ability to fine-tune the fields in a microfluidic device will be cost-effective since one device can be tested for multiple analytes. Finally, manipulating small-size analytes by DEP will be achieved without applying high electric potentials.

CHAPTER 5

CONCLUSION AND FUTURE DIRECTIONS

In summary, two microfluidic platforms were presented for the manipulation of particles. In Chapter 3, the ratchet device demonstrated the separation of 0.27 and 0.87 μm PS particles. The large particles demonstrated ratchet migration, and the small particles demonstrated normal migration, effectively steering the two particle species into opposing directions. The large particle showed some deviation from the numerical model. This systematic error can be attributed to the fact that the PDF was not the same throughout experimentation. However, the ratchet migration was in good agreement with the numerical model showing that by increasing U_{dc} , the average velocities of the large particles decrease. It was noted that changing U_{ac_1} did not affect the increase or decrease in average velocities. The small particles showed good agreement with the numerical model. It was noted that the velocities of the particle increase when increasing U_{dc} . In addition, different ratchet designs were introduced for high throughput separation. In the future, the new ratchet design will be tested experimentally with beads and mitochondria. Numerical models will be adapted to aid in the experimental work. This work is crucial in developing high throughput microfluidic devices for separating organelles by size for biomolecular assessment.

Chapter 4 introduces a normally-closed valve that acts as an insulating dynamic constriction when applied to an electric potential. This chapter demonstrated the tunability of the valve and the electric field gradients by a COMSOL model and experimental work. The model demonstrated the tunability of the gradients by calculating the electric field gradient of different d_{gap} in a range from 0.1 to 10 μm . Similarly, two

pressure studies were conducted to understand the tunability of the valve experimentally. The first study demonstrated that higher aspect ratios required less vacuum to actuate the valve. The second study estimated the d_{gap} reached by different valves at certain vacuum pressures by correlating fluorescence intensities with distances achieved by the valve. Finally, the electric field gradient tunability was investigated by manipulating particles by iDEP at different pressures and potentials. The experiment demonstrated electric field tunability by the actuation of the valve. In the future, we aim to manipulate a PS bead mixture and biomolecules. In addition, new valve geometries will be explored to fine-tune the d_{gap} to reach nm distances. In summary, this thesis presents microfluidic platforms for the manipulation of analytes that in the future will aid in developing a new tool for analyte manipulation by DEP.

REFERENCES

1. Farzadfard, F.; Lu, T. K., Genomically Encoded Analog Memory with Precise in Vivo DNA Writing in Living Cell Populations. *Science* **2014**, *346* (6211), 825-832.
2. Boruah, K.; Dutta, J. C. In *Twenty Years of DNA Computing: From Complex Combinatorial Problems to the Boolean Circuits*, 2015 International Conference on Electronic Design, Computer Networks & Automated Verification (EDCAV), Shulong, India, 29-30 January 2015; IEEE: Shulong, India, 2015; pp 52-57.
3. Patten, P. A.; Howard, R. J.; Stemmer, W. P., Applications of DNA Shuffling to Pharmaceuticals and Vaccines. *Curr. Opin. Biotech.* **1997**, *8* (6), 724-733.
4. Azizgolshani, N.; Petersen, C. L.; Chen, Y.; Levy, J. J.; Salas, L. A.; Perreard, L.; Nguyen, L. N.; Christensen, B. C., DNA 5-hydroxymethylcytosine in Pediatric Central Nervous System Tumors May Impact Tumor Classification and is a Positive Prognostic Marker. *Clin. Epigenetics.* **2021**, *13* (1), 1-17.
5. Li, J.; Feng, Z.; Wang, J.; Huang, G.; Yan, L., Interaction of Aflatoxin G1 with Free DNA in Vitro and Possibility of its Application in Removing Aflatoxin G1. *J. Environ. Sci. Health B* **2021**, 1-9.
6. Lee, P. Y.; Costumbrado, J.; Hsu, C. Y.; Kim, Y. H., Agarose Gel Electrophoresis for the Separation of DNA Fragments. *J. Vis. Exp.* **2012**, (62).
7. Shokouhmand, H.; Abdollahi, A., Detection of Cell-free DNA Nanoparticles in Insulator-based Dielectrophoresis Systems. *J. Chromatogr. A* **2020**, *1626*, 1-10.
8. Oh, M.; Jayasooriya, V.; Woo, S. O.; Nawarathna, D.; Choi, Y., Selective Manipulation of Biomolecules with Insulator-Based Dielectrophoretic Tweezers. *ACS. Appl. Nano Mater.* **2020**, *3* (1), 797-805.
9. Holzel, R., Dielectric and Dielectrophoretic Properties of DNA. *IET. Nanobiotechnol.* **2009**, *3* (2), 28-45.
10. Zhao, H., Role of Hydrodynamic Behavior of DNA Molecules in Dielectrophoretic Polarization Under the Action of an Electric Field. *Phys. Rev. E.* **2011**, *84* (2), 1-6.

11. Regtmeier, J.; Eichhorn, R.; Bogunovic, L.; Ros, A.; Anselmetti, D., Dielectrophoretic Trapping and Polarizability of DNA: The Role of Spatial Conformation. *Anal. Chem.* **2010**, *82* (17), 7141-7149.
12. Viefhues, M.; Regtmeier, J.; Anselmetti, D., Fast and Continuous-flow Separation of DNA-complexes and Topological DNA Variants in Microfluidic Chip Format. *Analyst* **2013**, *138* (1), 186-196.
13. Gallo-Villanueva, R. C.; Rodríguez-López, C. E.; Díaz-de-la-Garza, R. I.; Reyes-Betanzo, C.; Lapizco-Encinas, B. H., DNA Manipulation by Means of Insulator-Based Dielectrophoresis Employing Direct Current Electric Fields. *Electrophoresis* **2009**, *30* (24), 4195-4205.
14. Saucedo-Espinosa, M. A.; Lapizco-Encinas, B. H., Design of Insulator-Based Dielectrophoretic Devices: Effect of Insulator Posts Characteristics. *J. Chromatogr. A* **2015**, *1422*, 325-333.
15. Sabbagh, B.; Stolovicki, E.; Park, S.; Weitz, D. A.; Yossifon, G., Tunable Nanochannels Connected in Series for Dynamic Control of Multiple Concentration-Polarization Layers and Preconcentrated Molecule Plugs. *Nano. Lett.* **2020**, *20* (12), 8524-8533.
16. Kwon, H. J.; Hong, S. K.; Lee, M.; Lim, G., An On-Demand Micro/Nano-Convertible Channel Using an Elastomeric Nanostructure for Multi-purpose Use. *Lab Chip* **2019**, *19* (18), 2958-2965.
17. Abou-Sleiman, P. M.; Muqit, M. M.; Wood, N. W., Expanding Insights of Mitochondrial Dysfunction in Parkinson's Disease. *Nat. Rev. Neurosci.* **2006**, *7* (3), 207-219.
18. Fernández-Vizarra, E.; López-Pérez, M. J.; Enriquez, J. A., Isolation of Biogenetically Competent Mitochondria from Mammalian Tissues and Cultured Cells. *Methods* **2002**, *26* (4), 292-297.
19. Michelsen, U.; von Hagen, J., Chapter 19 Isolation of Subcellular Organelles and Structures. In *Guide to Protein Purification, 2nd Edition*, 2009; pp 305-328.
20. Hänggi, P.; Marchesoni, F., Artificial Brownian Motors: Controlling Transport on the Nanoscale. *Rev. Mod. Phys.* **2009**, *81* (1), 387-442.

21. Lau, B.; Kedem, O.; Schwabacher, J.; Kwasnieski, D.; Weiss, E. A., An Introduction to Ratchets in Chemistry and Biology. *Mater. Horiz.* **2017**, *4* (3), 310-318.
22. Kim, D.; Luo, J.; Arriaga, E. A.; Ros, A., Deterministic Ratchet for Sub-micrometer (Bio)particle Separation. *Anal. Chem.* **2018**, *90* (7), 4370-4379.
23. Doering, C. R.; Gibbon, J. D., *Applied analysis of the Navier-Stokes Equations*. Cambridge University Press: 1995.
24. Lee, H.; Ham, D.; Westervelt, R. M., *CMOS Biotechnology*. Springer: 2007.
25. Ostadfar, A., *Biofluid Mechanics: Principles and Applications*. Academic Press: 2016.
26. Sonker, M.; Kim, D.; Egatz-Gomez, A.; Ros, A., Separation Phenomena in Tailored Micro- and Nanofluidic Environments. *Annu. Rev. Anal. Chem.* **2019**, *12* (1), 475-500.
27. Tandon, V.; Bhagavatula, S. K.; Nelson, W. C.; Kirby, B. J., Zeta Potential and Electroosmotic Mobility in Microfluidic Devices Fabricated from Hydrophobic Polymers: 1. The Origins of Charge. *Electrophoresis* **2008**, *29* (5), 1092-1101.
28. Kleinstreuer, C., *Microfluidics and Nanofluidics: Theory and Selected Applications*. John Wiley & Sons: 2013.
29. Hellmich, W.; Regtmeier, J.; Duong, T. T.; Ros, R.; Anselmetti, D.; Ros, A., Poly(oxyethylene) Based Surface Coatings for Poly(dimethylsiloxane) Microchannels. *Langmuir* **2005**, *21* (16), 7551-7557.
30. García, C. D.; Chumbimuni-Torres, K. Y.; Carrilho, E., *Capillary Electrophoresis and Microchip Capillary Electrophoresis: Principles, Applications, and Limitations*. John Wiley & Sons: 2013.
31. Rodriguez, M. A.; Armstrong, D. W., Separation and Analysis of Colloidal/Nano-Particles Including Microorganisms by Capillary Electrophoresis: A Fundamental Review. *J. Chromatogr. B Analyt.* **2004**, *800* (1-2), 7-25.

32. Mitra, S. K.; Chakraborty, S., *Microfluidics and Nanofluidics Handbook: Chemistry, Physics, and Life Science Principles*. CRC Press: 2011.
33. Ohshima, H., *Theory of Colloid and Interfacial Electric Phenomena*. Academic Press: Netherlands, 2006.
34. Jones, T. B., *Electromechanics of Particles*. Cambridge University Press: 2005.
35. Pohl, H. A.; Crane, J. S., Dielectrophoretic Force. *J. Theor. Biol.* **1972**, *37* (1), 1-13.
36. Gautam, M.; Jara, J. H.; Sekerkova, G.; Yasvoina, M. V.; Martina, M.; Ozdinler, P. H., Absence of Alsln Function Leads to Corticospinal Motor Neuron Vulnerability Via Novel Disease Mechanisms. *Hum. Mol. Genet.* **2016**, *25* (6), 1074-87.
37. Somani, P.; Simon, V. A.; Temesy-Armos, P. N.; Gross, S. A.; Didio, L. J., Amiodarone-Associated Changes in Human Neutrophils. *Am. J. Cardiol.* **1986**, *57* (8), 666-672.
38. Zhu, H.; Li, H.; Wang, P.; Chen, M.; Huang, Z.; Li, K.; Li, Y.; He, J.; Han, J.; Zhang, Q., Persistent and Acute Chlamydial Infections Induce Different Structural Changes in the Golgi Apparatus. *Int. J. Med. Microbiol.* **2014**, *304* (5-6), 577-85.
39. Tan, X.; Banerjee, P.; Guo, H. F.; Ireland, S.; Pankova, D.; Ahn, Y. H.; Nikolaidis, I. M.; Liu, X.; Zhao, Y.; Xue, Y.; Burns, A. R.; Roybal, J.; Gibbons, D. L.; Zal, T.; Creighton, C. J.; Ungar, D.; Wang, Y.; Kurie, J. M., Epithelial-to-Mesenchymal Transition Drives a Pro-metastatic Golgi Compaction Process Through Scaffolding Protein PAQR11. *J. Clin. Invest.* **2017**, *127* (1), 117-131.
40. Saita, S.; Ishihara, T.; Maeda, M.; Iemura, S. i.; Natsume, T.; Mihara, K.; Ishihara, N., Distinct Types of Protease Systems are Involved in Homeostasis Regulation of Mitochondrial Morphology Via Balanced Fusion and Fission. *Genes Cells* **2016**, *21* (5), 408-424.
41. Shami, G. J.; Cheng, D.; Verhaegh, P.; Koek, G.; Wisse, E.; Braet, F., Three-Dimensional Ultrastructure of Giant Mitochondria in Human Non-Alcoholic Fatty Liver Disease. *Sci. Rep-UK.* **2021**, *11* (1), 1-14.

42. Navratil, M.; Terman, A.; Arriaga, E. A., Giant Mitochondria Do Not Fuse and Exchange Their Contents with Normal Mitochondria. *Exp. Cell. Res.* **2008**, *314* (1), 164-172.
43. Brown, T. A.; Fetter, R. D.; Tkachuk, A. N.; Clayton, D. A., Approaches Toward Super-Resolution Fluorescence Imaging of Mitochondrial Proteins Using PALM. *Methods* **2010**, *51* (4), 458-463.
44. Eguchi, M.; Iwama, Y.; Ochiai, F.; Ishikawa, K.; Sakakibara, H.; Sakamaki, H.; Furukawa, T., Giant Mitochondria in Acute Lymphocytic Leukemia. *Exp. Mol. Pathol.* **1987**, *47* (1), 69-75.
45. Filippone, E. J.; Farber, J. L., The Specificity of Acute and Chronic Microvascular Alterations in Renal Allografts. *Clin. Transplant.* **2013**, *27* (6), 790-798.
46. Storrie, B.; Amadden, E., Isolation of Subcellular Organelles. *Method. Enzymol.* **1990**, *182*, 203-225.
47. Strack, A.; Duffy, C. F.; Malvey, M.; Arriaga, E. A., Individual Mitochondrion Characterization: A Comparison of Classical Assays to Capillary Electrophoresis with Laser-Induced Fluorescence Detection. *Anal. Biochem.* **2001**, *294* (2), 141-147.
48. Hartwig, S.; Feckler, C.; Lehr, S.; Wallbrecht, K.; Wolgast, H.; Muller-Wieland, D.; Kotzka, J., A Critical Comparison Between Two Classical and a Kit-Based Method for Mitochondria Isolation. *Proteomics* **2009**, *9* (11), 3209-3214.
49. McDonald, T.; Sheng, S.; Stanley, B.; Chen, D.; Ko, Y.; Cole, R. N.; Pedersen, P.; Van Eyk, J. E., Expanding the Subproteome of the Inner Mitochondria Using Protein Separation Technologies: One- and Two-Dimensional Liquid Chromatography and Two-Dimensional Gel Electrophoresis. *Mol. Cell. Proteomics* **2006**, *5* (12), 2392-2411.
50. Moschallski, M.; Hausmann, M.; Posch, A.; Paulus, A.; Kunz, N.; Duong, T. T.; Angres, B.; Fuchsberger, K.; Steuer, H.; Stoll, D.; Werner, S.; Hagemeyer, B.; Stelzle, M., MicroPrep: Chip-Based Dielectrophoretic Purification of Mitochondria. *Electrophoresis* **2010**, *31* (15), 2655-2663.

51. Presley, A. D.; Fuller, K. M.; Arriaga, E. A., MitoTracker Green Labeling of Mitochondrial Proteins and their Subsequent Analysis by Capillary Electrophoresis with Laser-Induced Fluorescence Detection. *J. Chromatogr. B* **2003**, *793* (1), 141-150.
52. Kim, D.; Sonker, M.; Ros, A., Dielectrophoresis: From Molecular to Micrometer-Scale Analytes. *Anal. Chem.* **2019**, *91* (1), 277-295.
53. Korensky, G.; Chen, X.; Bao, M.; Miller, A.; Lapizco-Encinas, B.; Park, M.; Du, K., Single Chlamydomonas Reinhardtii Cell Separation from Bacterial Cells and Auto-Fluorescence Tracking with a Nanosieve Device. *Electrophoresis* **2020**, *42* (1-2), 95-102.
54. Coll De Pena, A.; Miller, A.; Lentz, C. J.; Hill, N.; Parthasarathy, A.; Hudson, A. O.; Lapizco-Encinas, B. H., Creation of an Electrokinetic Characterization Library for the Detection and Identification of Biological Cells. *Anal. Bioanal. Chem.* **2020**, *412* (16), 3935-3945.
55. Liu, Y.; Hayes, M. A., Differential Biophysical Behaviors of Closely Related Strains of Salmonella. *Front. Microbiol.* **2020**, *11* (302), 1-8.
56. Jones, P. V.; Salmon, G. L.; Ros, A., Continuous Separation of DNA Molecules by Size Using Insulator-Based Dielectrophoresis. *Anal. Chem.* **2017**, *89* (3), 1531-1539.
57. Camacho-Alanis, F.; Gan, L.; Ros, A., Transitioning Streaming to Trapping in DC Insulator-Based Dielectrophoresis for Biomolecules. *Sensor. Actuat. B-Chem.* **2012**, *173*, 668-675.
58. Gan, L.; Chao, T. C.; Camacho-Alanis, F.; Ros, A., Six-Helix Bundle and Triangle DNA Origami Insulator-Based Dielectrophoresis. *Anal. Chem.* **2013**, *85* (23), 11427-11434.
59. Viefhues, M.; Eichhorn, R., DNA Dielectrophoresis: Theory and Applications a Review. *Electrophoresis* **2017**, *38* (11), 1483-1506.
60. Liu, Y.; Hayes, M. A., Orders-of-Magnitude Larger Force Demonstrated for Dielectrophoresis of Proteins Enabling High-Resolution Separations Based on New Mechanisms. *Anal. Chem.* **2021**, *93* (3), 1352-1359.

61. Nakano, A.; Camacho-Alanis, F.; Ros, A., Insulator-Based Dielectrophoresis with Beta-Galactosidase in Nanostructured Devices. *Analyst* **2015**, *140* (3), 860-868.
62. Nakano, A.; Chao, T. C.; Camacho-Alanis, F.; Ros, A., Immunoglobulin G and Bovine Serum Albumin Streaming Dielectrophoresis in a Microfluidic Device. *Electrophoresis* **2011**, *32* (17), 2314-2322.
63. Nakano, A.; Ros, A., Protein Dielectrophoresis: Advances, Challenges, and Applications. *Electrophoresis* **2013**, *34* (7), 1085-1096.
64. Rabbani, M. T.; Schmidt, C. F.; Ros, A., Length-Selective Dielectrophoretic Manipulation of Single-Walled Carbon Nanotubes. *Anal. Chem.* **2020**, *92* (13), 8901-8908.
65. Rabbani, M. T.; Schmidt, C. F.; Ros, A., Single-Walled Carbon Nanotubes Probed with Insulator-Based Dielectrophoresis. *Anal. Chem.* **2017**, *89* (24), 13235-13244.
66. Rabbani, M. T.; Sonker, M.; Ros, A., Carbon Nanotube Dielectrophoresis: Theory and Applications. *Electrophoresis* **2020**, *41* (21-22), 1893-1914.
67. Wu, Y.; Ren, Y.; Tao, Y.; Hou, L.; Jiang, H., High-Throughput Separation, Trapping, and Manipulation of Single Cells and Particles by Combined Dielectrophoresis at a Bipolar Electrode Array. *Anal. Chem.* **2018**, *90* (19), 11461-11469.
68. Tajik, P.; Saidi, M. S.; Kashaninejad, N.; Nguyen, N.-T., Simple, Cost-Effective, and Continuous 3D Dielectrophoretic Microchip for Concentration and Separation of Bioparticles. *Ind. Eng. Chem. Res.* **2019**, *59* (9), 3772-3783.
69. Jiang, A. Y. L.; Yale, A. R.; Aghaamoo, M.; Lee, D. H.; Lee, A. P.; Adams, T. N. G.; Flanagan, L. A., High-Throughput Continuous Dielectrophoretic Separation of Neural Stem Cells. *Biomicrofluidics* **2019**, *13*, 064111.
70. Stoop, R. L.; Straube, A. V.; Tierno, P., Enhancing Nanoparticle Diffusion on a Unidirectional Domain Wall Magnetic Ratchet. *Nano. Lett.* **2019**, *19* (1), 433-440.
71. Schindelin, J.; Arganda-Carreras, I.; Frise, E.; Kaynig, V.; Longair, M.; Pietzsch, T.; Preibisch, S.; Rueden, C.; Saalfeld, S.; Schmid, B.; Tinevez, J. Y.;

White, D. J.; Hartenstein, V.; Eliceiri, K.; Tomancak, P.; Cardona, A., Fiji: An Open-Source Platform for Biological-Image Analysis. *Nat. Methods* **2012**, *9* (7), 676-682.

72. Sbalzarini, I. F.; Koumoutsakos, P., Feature Point Tracking and Trajectory Analysis for Video Imaging in Cell Biology. *J. Struct. Biol.* **2005**, *151* (2), 182-195.

73. Kim, D. H. Electric Field Driven Migration and Separation in the Microenvironment. PhD. Dissertation, Arizona State University, Tempe, AZ, 2020.

74. Lapizco-Encinas, B. H., On the Recent Developments of Insulator-Based Dielectrophoresis: A Review. *Electrophoresis* **2019**, *40* (3), 358-375.

75. Gallo-Villanueva, R. C.; Perez-Gonzalez, V. H.; Cardenas-Benitez, B.; Jind, B.; Martinez-Chapa, S. O.; Lapizco-Encinas, B. H., Joule Heating Effects in Optimized Insulator-Based Dielectrophoretic Devices: An Interplay Between Post Geometry and Temperature Rise. *Electrophoresis* **2019**, *40* (10), 1408-1416.

76. Nakano, A.; Luo, J.; Ros, A., Temporal and Spatial Temperature Measurement in Insulator-Based Dielectrophoretic Devices. *Anal. Chem.* **2014**, *86* (13), 6516-6524.

77. Ying, L.; Bruckbauer, A.; Rothery, A. M.; Korchev, Y. E.; Klenerman, D., Programmable Delivery of DNA Through a Nanopipet. *Anal. Chem.* **2002**, *74* (6), 1380-1385.

78. Ying, L.; White, S. S.; Bruckbauer, A.; Meadows, L.; Korchev, Y. E.; Klenerman, D., Frequency and Voltage Dependence of the Dielectrophoretic Trapping of Short Lengths of DNA and dCTP in a Nanopipette. *Biophys. J.* **2004**, *86* (2), 1018-1027.

79. Hashiguchi, G.; Goda, T.; Hosogi, M.; Hirano, K.; Kaji, N.; Baba, Y.; Kakushima, K.; Fujita, H., DNA Manipulation and Retrieval From an Aqueous Solution with Micromachined Nanotweezers. *Anal. Chem.* **2003**, *75* (17), 4347-4350.

80. Kumemura, M.; Collard, D.; Sakaki, N.; Yamahata, C.; Hosogi, M.; Hashiguchi, G.; Fujita, H., Single-DNA-Molecule Trapping With Silicon Nanotweezers Using Pulsed Dielectrophoresis. *J. Micromech. Microeng.* **2011**, *21* (5), 054020.

81. Viefhues, M.; Regtmeier, J.; Anselmetti, D., Nanofluidic Devices for Dielectrophoretic Mobility Shift Assays by Soft Lithography. *J. Micromech. Microeng.* **2012**, *22* (11), 115024.
82. Viefhues, M.; Wegener, S.; Rischmüller, A.; Schleef, M.; Anselmetti, D., Dielectrophoresis Based Continuous-Flow Nano Sorter: Fast Quality Control of Gene Vaccines. *Lab Chip* **2013**, *13* (15), 3111-3118.
83. Bruckbauer, A.; Ying, L.; Rothery, A. M.; Zhou, D.; Shevchuk, A. I.; Abell, C.; Korchev, Y. E.; Klenerman, D., Writing with DNA and Protein Using a Nanopipet for Controlled Delivery. *J. Am. Chem. Soc.* **2002**, *124* (30), 8810-8811.
84. Chaurey, V.; Rohani, A.; Su, Y. H.; Liao, K. T.; Chou, C. F.; Swami, N. S., Scaling Down Constriction-Based (Electrodeless) Dielectrophoresis Devices for Trapping Nanoscale Bioparticles in Physiological Media of High-Conductivity. *Electrophoresis* **2013**, *34* (7), 1097-1104.
85. Liao, K.-T.; Chou, C.-F., Nanoscale Molecular Traps and Dams for Ultrafast Protein Enrichment in High-Conductivity Buffers. *J. Am. Chem. Soc.* **2012**, *134* (21), 8742-8745.
86. Chiou, C.-H.; Chien, L.-J.; Kuo, J.-N., Nanoconstriction-Based Electrodeless Dielectrophoresis Chip for Nanoparticle and Protein Preconcentration. *Appl. Phys. Express* **2015**, *8* (8), 085201.
87. Gallo-Villanueva, R. C.; Sano, M. B.; Lapizco-Encinas, B. H.; Davalos, R. V., Joule Heating Effects on Particle Immobilization in Insulator-Based Dielectrophoretic Devices. *Electrophoresis* **2014**, *35* (2-3), 352-361.
88. Matsuura, Y.; Takehira, M.; Joti, Y.; Ogasahara, K.; Tanaka, T.; Ono, N.; Kunishima, N.; Yutani, K., Thermodynamics of Protein Denaturation at Temperatures Over 100 C: CutA1 Mutant Proteins Substituted with Hydrophobic and Charged Residues. *Sci. Rep-UK.* **2015**, *5* (1), 1-9.
89. Aghilinejad, A.; Aghaamoo, M.; Chen, X.; Xu, J., Effects of Electrothermal Vortices on Insulator-Based Dielectrophoresis for Circulating Tumor Cell Separation. *Electrophoresis* **2018**, *39* (5-6), 869-877.

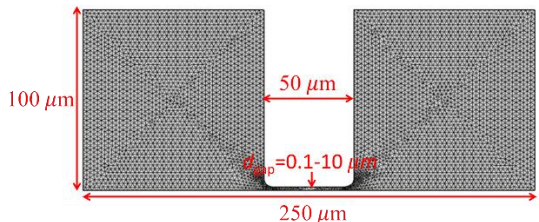
90. Hyler, A. R.; Hong, D.; Davalos, R. V.; Swami, N. S.; Schmelz, E. M., A Novel Ultralow Conductivity Electromanipulation Buffer Improves Cell Viability and Enhances Dielectrophoretic Consistency. *Electrophoresis* **2021**, *42* (12-13), 1366-1377.
91. Puttaswamy, S. V.; Sivashankar, S.; Chen, R. J.; Chin, C. K.; Chang, H. Y.; Liu, C. H., Enhanced Cell Viability and Cell Adhesion Using Low Conductivity Medium for Negative Dielectrophoretic Cell Patterning. *Biotechnol. J.* **2010**, *5* (10), 1005-1015.
92. Di Martino, R.; Camarda, M.; Cascio, M.; Gallo, M.; Magliano, A.; Baldo, S.; Romano, A.; Minafra, L.; Forte, G. I.; Russo, G., Analysis of the Role of Elution Buffers on the Separation Capabilities of Dielectrophoretic Devices. *Sens. Bio-Sens* **2016**, *7*, 162-167.
93. Zhao, H.; Stanley, K.; Wu, Q. J.; Czyzewska, E., Structure and Characterization of a Planar Normally Closed Bulk-Micromachined Piezoelectric Valve for Fuel Cell Applications. *Sensor. Actuat. A-Phys* **2005**, *120* (1), 134-141.
94. Hosokawa, K.; Maeda, R., A Pneumatically-Actuated Three-Way Microvalve Fabricated with Polydimethylsiloxane Using the Membrane Transfer Technique. *J. Micromech. Microeng.* **2000**, *10* (3), 415.
95. Lee, D. E.; Soper, S.; Wang, W., Design and Fabrication of an Electrochemically Actuated Microvalve. *Microsys. Technol.* **2008**, *14* (9-11), 1751-1756.
96. Kaigala, G. V.; Hoang, V. N.; Backhouse, C. J., Electrically Controlled Microvalves to Integrate Microchip Polymerase Chain Reaction and Capillary Electrophoresis. *Lab. Chip.* **2008**, *8* (7), 1071-10788.
97. Jacobson, S. C.; Ermakov, S. V.; Ramsey, J. M., Minimizing the Number of Voltage Sources and Fluid Reservoirs for Electrokinetic Valving in Microfluidic Devices. *Anal. Chem.* **1999**, *71* (15), 3273-3276.
98. Pemble, C. M.; Towe, B. C., A Miniature Shape Memory Alloy Pinch Valve. *Sensor. Actuat. A-Phys.* **1999**, *77* (2), 145-148.
99. Weibel, D. B.; Kruithof, M.; Potenta, S.; Sia, S. K.; Lee, A.; Whitesides, G. M., Torque-Actuated Valves for Microfluidics. *Anal. Chem.* **2005**, *77* (15), 4726-4733.

100. Weibel, D. B.; Siegel, A. C.; Lee, A.; George, A. H.; Whitesides, G. M., Pumping Fluids in Microfluidic Systems Using the Elastic Deformation of Poly(dimethylsiloxane). *Lab Chip* **2007**, *7* (12), 1832-1836.
101. Sundararajan, N.; Kim, D.; Berlin, A. A., Microfluidic Operations Using Deformable Polymer Membranes Fabricated by Single Layer Soft Lithography. *Lab Chip* **2005**, *5* (3), 350-354.
102. Studer, V.; Hang, G.; Pandolfi, A.; Ortiz, M.; French Anderson, W.; Quake, S. R., Scaling Properties of a Low-Actuation Pressure Microfluidic Valve. *J. Appl. Phys.* **2004**, *95* (1), 393-398.
103. Cong, Y.; Katipamula, S.; Geng, T.; Prost, S. A.; Tang, K.; Kelly, R. T., Electrokinetic Sample Preconcentration and Hydrodynamic Sample Injection for Microchip Electrophoresis Using a Pneumatic Microvalve. *Electrophoresis* **2016**, *37* (3), 455-462.
104. Ros, A.; Kim, D.; Luo, J.; Yang, M. Tunable Insulator-Based Dielectrophoresis (iDEP) with Membrane Valves. 2019.
105. Mohan, R.; Schudel, B. R.; Desai, A. V.; Yearsley, J. D.; Ablett, C. A.; Kenis, P. J. A., Design Considerations for Elastomeric Normally Closed Microfluidic Valves. *Sensor. Actuat. B-Chem.* **2011**, *160* (1), 1216-1223.
106. Yang, M.; Cruz Villarreal, J.; Ariyasinghe, N.; Kruithoff, R.; Ros, R.; Ros, A., Quantitative Approach for Protein Analysis in Small Cell Ensembles by an Integrated Microfluidic Chip with MALDI Mass Spectrometry. *Anal. Chem.* **2021**, *93* (15), 6053-6061.
107. Yang, M.; Nelson, R.; Ros, A., Toward Analysis of Proteins in Single Cells: A Quantitative Approach Employing Isobaric Tags with MALDI Mass Spectrometry Realized with a Microfluidic Platform. *Anal. Chem.* **2016**, *88* (13), 6672-6679.
108. Szydzik, C.; Brazilek, R. J.; Khoshmanesh, K.; Akbaridoust, F.; Knoerzer, M.; Thurgood, P.; Muir, I.; Marusic, I.; Nandurkar, H.; Mitchell, A.; Nesbitt, W. S., Elastomeric Microvalve Geometry Affects Haemocompatibility. *Lab Chip* **2018**, *18* (12), 1778-1792.

109. Modarres, P.; Tabrizian, M., Alternating Current Dielectrophoresis of Biomacromolecules: The Interplay of Electrokinetic Effects. *Sensor. Actuat. B-Chem.* **2017**, *252*, 391-408.
110. Hayes, M. A., Dielectrophoresis of Proteins: Experimental Data and Evolving Theory. *Anal. Bioanal. Chem.* **2020**, *412* (16), 3801-3811.
111. Swami, N.; Chou, C.-F.; Ramamurthy, V.; Chaurey, V., Enhancing DNA Hybridization Kinetics Through Constriction-Based Dielectrophoresis. *Lab Chip* **2009**, *9* (22), 3212-3220.
112. Sano, H.; Kabata, H.; Kurosawa, O.; Washizu, M. In *Dielectrophoretic Chromatography with Cross-Flow Injection*, Technical Digest. MEMS 2002 IEEE International Conference. Fifteenth IEEE International Conference on Micro Electro Mechanical Systems (Cat. No. 02CH37266), IEEE: 2002; pp 11-14.
113. Liao, K. T.; Tsegaye, M.; Chaurey, V.; Chou, C. F.; Swami, N. S., Nano-Constriction Device for Rapid Protein Preconcentration in Physiological Media Through a Balance of Electrokinetic Forces. *Electrophoresis* **2012**, *33* (13), 1958-1966.
114. Nouri-Goushki, M.; Mirzaali, M.; Angeloni, L.; Fan, D.; Minneboo, M.; Ghatkesar, M.; Staufer, U.; Fratila-Apachitei, L.; Zadpoor, A., 3D Printing of Large Areas of Highly Ordered Submicron Patterns for Modulating Cell Behavior. *ACS Appl. Mater. Interfaces* **2019**, *12* (1), 200-208.

APPENDIX A

COMSOL SIMULATION DETAIL FOR CHAPTER 4

| Items | Variables | Detailed Description |
|-----------|-----------------------------------|--|
| Parameter | Electric Potential, V_0 | 25 V, Calculated from $(1000 \text{ V/cm})(0.025 \mu\text{m})=25 \text{ V}$ |
| | Electrical conductivity, σ | 0.03 [S/m] |
| | Relative permittivity | 80.2 |
| | Dynamic viscosity | 0.001158 [Pa*s] |
| | Density | 997.0479[kg/m ³] |
| Geometry | Mesh: Extremely Fine |  |